

A vector Helmholtz electromagnetic wave propagator for inhomogeneous media

Laurence Keefe*, Austin McDaniel, Max Cubillos, Ilya Zilberter,†
Timothy Madden

Air Force Research Laboratory, 3550 Aberdeen Ave SE, Kirtland AFB, New Mexico 87117, USA

Abstract

The vector electric-field Helmholtz equation, containing cross-polarization terms, is factored to produce both pseudo-differential and exponential operator forms of a three-dimensional, one-way, vector, wave equation for propagation through inhomogeneous media. From this operator factorization we develop a high-order approximate, vector Helmholtz propagator that correctly handles forward-arc, high-angle scattering and diffraction from inhomogeneities at all resolved length scales, and seamlessly includes evanescent waves.

Our implementation of the exponential operator form of the one-way propagator is discussed extensively. A rational approximation/partial fraction decomposition of the exponential operator converts the propagator into a moderate number of large, sparse, linear solves whose results are summed together at each step to advance the electric field in space. We use a new AAA-Lawson rational interpolant for this approximation, rather than the more common Padé expansions that have appeared in the seismic and ocean acoustics literature previously. GMRES is used to solve these large systems. A direct-solve, free space propagation method proves to be an effective preconditioner for GMRES, but can also serve as a standalone propagator in homogeneous media. Scalar computational examples shown include plane wave diffraction by a circular aperture and Gaussian beam propagation through sine-product and homogeneous refractive index fields. The sine-product example compares its results to that of paraxial propagation through the same media, and demonstrates the substantial differences between these propagator paradigms when the scale of the inhomogeneities is of the order of the fundamental wavelength in the Helmholtz equation. We also examine the convergence of the homogeneous media beam results to fields generated by Clenshaw-Curtis evaluation of the first Rayleigh-Sommerfeld integral for the same initial conditions.

1 Introduction

There are many computational alternatives for simulating the propagation of electromagnetic (EM) waves, differentiated by both the mathematical character of their formulation and the computational complexity of their implementation. In time-dependent problems the Finite-Difference-Time-Domain (FDTD) method [45] applied to (the hyperbolic system of) Maxwell's equations is one standard. Such initial boundary value problems require fine spatial grids for accuracy and stability, minute time integration steps to capture transient behaviors, and the ability to implement an application-dependent range of boundary conditions (Dirichlet, Neumann, Robin/impedance, non-reflecting). Computational resource demands are high. For single-frequency/continuous-wave applications (e.g. radar cross-section calculations), integrations/simulations of the (elliptical) scalar Helmholtz equation are preferred. Time integration is absent, but the spatial gridding

*National Research Council Senior Research Associate. Current address: Zebara LLC, Albuquerque, New Mexico 87104

†National Research Council Research Associate. Current address: Tech-X, Boulder, Colorado 80303

requirements remain, and boundary condition versatility is still a necessity. In addition, these are boundary value problems that require a whole field solution, and iterative techniques are likely necessary as grid sizes become large and direct solution techniques become unwieldy. When backscatter can be neglected, and continuous-wave propagation is in the forward-arc, there are one-way propagators, a subset of Helmholtz methods. They are either exact or approximate scalar integral solutions (Rayleigh-Sommerfeld, Fresnel, Fraunhofer, or their Fourier-transform equivalent Angular Spectrum methods) valid only in homogeneous media, or (parabolic) one-way wave equations that can be used in either homogeneous or inhomogeneous media. One-way propagators are the simplest computationally, because the formulations of the integrals and the one-way wave equations allow solutions to be constructed on isolated or successive coordinate surfaces normal to a predominant propagation direction, rather than requiring a whole field solution over the entire physical domain. Boundary conditions need only be applied in two transverse dimensions, and there is no necessity for a terminating boundary condition on the final surface of the solution. The original one-way wave equation in this class is the paraxial equation, derived by Leontovich and Fock (L&F) [25] in 1946 for the study of long range radio propagation near the Earth's surface. It is a low-wavenumber approximation of the scalar Helmholtz equation for scenarios where there is a distinguished/primary propagation direction. The L&F approximation was not created with numerical computation in mind, but its advantages over the Helmholtz equation in this respect were soon appreciated. It became the mainstay for computations of radio wave propagation both parallel and normal to the Earth [26, 22], and spread to simulations of light/laser beam propagation in turbulent atmospheres [41, 42, 39, 2], seismic waves in the Earth [8], and ocean acoustics [40]. The current work falls into the one-way propagator class, but is neither a scalar integral solution nor a version of the scalar paraxial equation.

The new tool we introduce here is directed towards the study of vector electromagnetic (EM) wave propagation in inhomogeneous media. In this paper we describe the theory and numerical procedures underlying a one-way wave equation propagator that results from a particular factorization of the vector electromagnetic Helmholtz equation

$$\nabla^2 \mathbf{E} + \nabla \left(\frac{1}{n^2} \mathbf{E} \cdot \nabla n^2 \right) + k_0^2 n^2 \mathbf{E} = 0 . \quad (1)$$

The derivation of this equation from Maxwell's equations will be recapitulated briefly in Section 2 of this paper, but a more thorough discussion of this general result, and the natural appearance of the cross-polarization term, can be found in standard texts [29, 30, 23, 6]. Our new propagator extends the phenomenological domain of diffraction studies beyond that described by the scalar three-dimensional Helmholtz equation, and provides for the continuous coupling of electric field components throughout the media, not just at boundaries and/or scatterers. This one-way wave equation accurately propagates all forward-arc waves described by the Helmholtz wavenumber dispersion relation. These include scattered and diffracted waves at all resolved wavenumbers below the Helmholtz cutoff, $k \leq k_0 n$, as well as highly damped evanescent waves at wavenumbers beyond the Helmholtz cutoff boundary. This distinguishes it from the paraxial equation, whose wavenumber dispersion relation is a low-wavenumber quadratic approximation to the Helmholtz dispersion relation, and consequently does not allow for evanescent waves. We expect this new tool to be particularly appropriate for simulation of wave propagation through refractive index fields with high-wavenumber content, as well as for initial conditions with spatial support having wavelength or smaller scales.

Though the emphasis of our new propagator is vector electric field propagation in inhomogeneous media, it contains a new scalar propagator for homogeneous media, $n(x, y, z) = n_0$, that solves

$$\Delta u + (k_0 n_0)^2 u = 0 \quad (2)$$

via methods different from those integral techniques (Fourier transform, quadratures) typically found in texts and the literature. Equation (2) is one of the fundamental field equations of mathematical physics. It appears

naturally as an idealization of single frequency wave propagation in fluid (atmospheric and oceanic) acoustics and seismology, and is easily derived for electromagnetic wave propagation from Maxwell's equations. In Cartesian coordinates its solution for outgoing waves in the $z \geq 0$ half-space, given a space-limited initial condition in the $z = 0$ plane, is the first Rayleigh-Sommerfeld (RS1) integral [14]

$$u_{RS1}(x, y, z) = -\frac{1}{2\pi} \iint_S \frac{z}{r} u(x', y', 0) \left(ik_0 n_0 - \frac{1}{r} \right) \frac{\exp(ik_0 n_0 r)}{r} dx' dy', \quad (3)$$

where

$$r = \sqrt{(x - x')^2 + (y - y')^2 + z^2} \quad (4)$$

is the distance between the point $(x', y', 0)$ in the source plane and the observation point at (x, y, z) , and S is the spatial region of the initial condition. It should be emphasized that the RS1 integral is a one-way propagator for scalar fields in homogeneous media.

In optics (3) has provided the theoretical basis for various quadrature schemes to solve homogeneous media diffraction problems within the plane-aperture framework of the RS1 analysis. These schemes have been tested [12, 13, 38, 44, 20] against the few canonical solutions to (3) that are known in the literature, primarily the analytical expression for the field and intensity on the centerline of a circular aperture [32]. Reference [27] is a contribution to the RS1 literature in the last decade that favors accuracy and computational efficiency in the intermediate range between near-field and far-field over near-field capability. It achieves this by restricting initial conditions to those with finite support in both spatial and wavenumber domains. In so doing it acquires the ability to calculate solutions out to ranges of a few millions of wavelengths, a distance that none of the other RS1 techniques have attempted. Most recently, [11] describes a method for computing the RS1 integral using sinc series approximation. Once certain quadrature weights are precomputed numerically, the accuracy of the quadrature does not depend on wavelength or propagation distance, only on how well the optical field is approximated by the sinc series. In Section 5 of the paper we will use Clenshaw-Curtis quadrature [43] of (3) to produce reference solutions of various beam propagation scenarios to demonstrate the convergence behavior of our new propagator.

The idea of extracting a one-way wave equation from factoring a Helmholtz equation valid in inhomogeneous media comes from a framework developed for two-dimensional scalar wave propagation in seismology and ocean acoustics beginning more than 30 years ago [3, 17, 9, 10, 28, 19]. In the ocean, large relative variations in the refractive index cause wide-angle acoustic propagation due to refraction, and accurate calculation of such scenarios requires more accurate approximations to the Helmholtz equation than that provided by the low-wavenumber, angle-restricted paraxial equation. Researchers in this field developed a consistent, extendable procedure based upon factoring a two-dimensional Helmholtz equation, then rationally approximating the propagation operator in the resulting pseudo-differential equation. A two-term binomial expansion of the pseudo-differential propagation operator yields a paraxial equation at lowest order, but higher-order ($\sim 20 - 30$) rational approximants (Padé, interpolation, least-squares, etc.) of that same operator and its formally integrated exponential form accurately capture wave propagation described by the appropriate Helmholtz dispersion relation at all forward-arc angles.

Researchers in EM propagation also applied this then-new simulation framework [16, 37] to produce scalar one-way equations in homogeneous media (from a factorization of (2)), but their low-expansion-order, serial numerical implementations lagged the more accurate, efficient, and parallelizable formulations developed contemporaneously in ocean acoustics [10]. These latter methods applied to both homogeneous and inhomogeneous media, and we extend them here to three dimensions to apply to vector EM wave propagation described by (1). In our new treatment the electric field components are coupled continuously within the three-dimensional inhomogeneous media by the cross-polarization term in the vector Helmholtz equation, satisfy the more general displacement field divergence condition, $\nabla \cdot \mathcal{D} = 0$, and propagate accurately

within the entire forward arc. While our propagator method employs non-reflecting Perfectly Matched Layer boundary conditions in the transverse directions, Dirichlet, Neumann, or Robin conditions can be easily implemented.

Factoring the vector Helmholtz equation produces both pseudo-differential and exponential operator forms of a one-way, vector, wave equation valid in inhomogeneous media. For the exponential operator form of the one-way propagator, a rational approximation/partial fraction decomposition of the exponential operator converts the propagator into a moderate number of large, sparse, linear solves whose results are summed together at each step to advance the vector electric field in space. We use a new AAA-Lawson rational interpolant [31] for this approximation, with wider validity and generally greater accuracy than the more common Padé expansions that have appeared in the seismic and ocean acoustics literature previously. GMRES is used to solve these large systems. Our new method for solving (2) proves to be an effective preconditioner for GMRES, but also serves as the default propagator in homogeneous media. It is independent of the integral solution techniques usually applied to (2). The direct solve of these homogeneous media preconditioner problems is simplified by the demonstration that, in three dimensions, they can all be put in the form of a Sylvester equation, and solved by standard methods. Initial scalar computational examples include Helmholtz plane wave diffraction by a circular aperture, and Gaussian beam propagations in both homogeneous and high-wavenumber inhomogeneous media. The latter of these two beam simulations expose notable differences between the results of Helmholtz and paraxial propagations.

The paper is organized in five additional sections. Section 2 contains the major theoretical results. A brief derivation of the vector Helmholtz equation is presented first. Then the exponential operator and pseudo-differential equation forms of the new EM propagator are derived by factoring the vector Helmholtz equation, which highlights the importance of what will be denoted the $\bar{\mathbf{Z}}$ operator matrix in both the vector Helmholtz equation and propagators. A rational approximation/partial fraction expansion of the exponential operator form of the propagator converts it to a moderate number of independent, large, sparse linear solves, whose results are summed at each space step to advance the electric field in space. Section 3 covers three specific rational approximation ideas applicable to the decomposition of the exponential and pseudo-differential forms of the propagator into the sparse linear solves discussed in Section 2. Section 4 discusses the numerical methods employed to implement the propagator, including finite differencing, PML boundary conditions, and preconditioning ideas for the GMRES method applied to the sparse linear solves. Section 5 covers initial scalar computational results. The first is Helmholtz diffraction by a circular aperture, where we demonstrate the need for initial spatial resolution well beyond the evanescent boundary to obtain accurate results for axial values of the field and intensity; the second shows the convergence of Gaussian beam propagations to those generated by Clenshaw-Curtis quadrature of the Rayleigh-Sommerfeld integral; the last is Helmholtz and paraxial propagation of beams through artificially generated refractive index fields with high-wavenumber inhomogeneities. There we demonstrate the substantial differences between the two propagation methods when the inhomogeneities are on the same scale as the fundamental wavelength. Section 6 of the paper summarizes the overall theoretical and computational results.

2 Vector Helmholtz Equation and Two Forms of the Propagator

In a lossless, chargeless medium, Maxwell's equations for the electric displacement $\mathcal{D} = (\mathcal{D}_1, \mathcal{D}_2, \mathcal{D}_3)$, electric field $\mathcal{E} = (\mathcal{E}_1, \mathcal{E}_2, \mathcal{E}_3)$, magnetic field $\mathcal{B} = (\mathcal{B}_1, \mathcal{B}_2, \mathcal{B}_3)$, and magnetizing field $\mathcal{H} = (\mathcal{H}_1, \mathcal{H}_2, \mathcal{H}_3)$

are

$$\frac{\partial \mathcal{D}}{\partial t} = \nabla \times \mathcal{H} \quad (5a)$$

$$\frac{\partial \mathcal{B}}{\partial t} = -\nabla \times \mathcal{E} \quad (5b)$$

$$\nabla \cdot \mathcal{D} = 0 \quad (5c)$$

$$\nabla \cdot \mathcal{B} = 0. \quad (5d)$$

The constitutive relations $\mathcal{D} = \varepsilon \mathcal{E}$ and $\mathcal{B} = \mu \mathcal{H}$ are assumed, where ε and μ are the permittivity and permeability of the medium and $\mu = \mu_0$, the permeability of free space. The permittivity is typically expressed as $\varepsilon(\mathbf{r}) = \varepsilon_0 \varepsilon_r(\mathbf{r})$, where ε_0 is the permittivity of free space and ε_r is the relative permittivity, the ratio of the permittivity of the medium to the permittivity of free space.

Taking the curl of (5b) the electric field \mathcal{E} satisfies

$$\nabla \times \nabla \times \mathcal{E} = -\mu_0 \varepsilon_0 \varepsilon_r(\mathbf{r}) \frac{\partial^2 \mathcal{E}}{\partial t^2}. \quad (6)$$

Assuming harmonic time-dependence, $\mathcal{E}(t, \mathbf{r}) = e^{i\omega t} \mathbf{E}(\mathbf{r})$, and utilizing the vector identity $\nabla \times \nabla \times \mathbf{E} = -\nabla^2 \mathbf{E} + \nabla(\nabla \cdot \mathbf{E})$, converts (6) into

$$\nabla^2 \mathbf{E} - \nabla(\nabla \cdot \mathbf{E}) = -\mu_0 \varepsilon_0 \varepsilon_r(\mathbf{r}) \omega^2 \mathbf{E}. \quad (7)$$

From Gauss' Law (5c),

$$\nabla \cdot \mathbf{E} = -\frac{\nabla \varepsilon}{\varepsilon} \cdot \mathbf{E} = -\frac{\nabla n^2}{n^2} \cdot \mathbf{E}, \quad (8)$$

where $n(\mathbf{r}) = \sqrt{\varepsilon_r(\mathbf{r})}$ is the refractive index. Then defining the vacuum wavenumber, $k_0 = \omega \sqrt{\mu_0 \varepsilon_0}$, we obtain the vector Helmholtz equation

$$\nabla^2 \mathbf{E} + \nabla \left(\frac{1}{n^2} \mathbf{E} \cdot \nabla n^2 \right) + k_0^2 n^2 \mathbf{E} = 0. \quad (9)$$

This vector, electric field, Helmholtz equation (9) forms the theoretical basis of the new propagator. The second term on the left-hand side describes the coupling of the components of the electric field and the resulting cross-polarization effects. There are many situations and applications where it has been argued that this term is negligible and can be dropped, thereby simplifying (9) to the scalar Helmholtz equation. However, for generality, we retain this term and work with the full vector Helmholtz equation (9).

The propagator derivation begins with the standard assumption that, over a single propagation step, the refractive index field varies only in the transverse directions, that is, $n^2 = n^2(x, y)$. The z -dependence of the refractive index is then accounted for by modifying the refractive index field between successive steps. In EM wave propagation, this assumption decouples the x, y electric field components (E_1, E_2) from the z -component E_3 , and plays a further crucial role in the structure and development of the propagator. If required, the E_3 component of the field can be recovered from (5c). An envelope assumption,

$$\mathbf{E}(x, y, z) = \mathbf{w}(x, y, z) e^{ik_0 n_0 z}, \quad (10)$$

with n_0 an arbitrary reference value of the refractive index, substituted into the vector Helmholtz equation (9), yields a vector equation for the z -evolution of the transverse components of the envelope electric field, $\hat{\mathbf{w}}(x, y, z) = [w_1(x, y, z), w_2(x, y, z)]^T$, over a single space step

$$\frac{d^2 \hat{\mathbf{w}}}{dz^2} + 2ik_0 n_0 \frac{d\hat{\mathbf{w}}}{dz} + k_0^2 n_0^2 \bar{\mathbf{Z}} \hat{\mathbf{w}} = 0. \quad (11)$$

Here \bar{Z} is the operator matrix,

$$\bar{Z} = \frac{1}{k_0^2 n_0^2} \begin{bmatrix} \Delta_{\perp} + k_0^2(n^2 - n_0^2) + \frac{\partial^2 \psi}{\partial x^2} + \frac{\partial \psi}{\partial x} \frac{\partial}{\partial x} & \frac{\partial^2 \psi}{\partial x \partial y} + \frac{\partial \psi}{\partial y} \frac{\partial}{\partial x} \\ \frac{\partial^2 \psi}{\partial x \partial y} + \frac{\partial \psi}{\partial x} \frac{\partial}{\partial y} & \Delta_{\perp} + k_0^2(n^2 - n_0^2) + \frac{\partial^2 \psi}{\partial y^2} + \frac{\partial \psi}{\partial y} \frac{\partial}{\partial y} \end{bmatrix}, \quad (12)$$

$\psi = \ln(n^2)$, and the transverse Laplacian is defined by $\Delta_{\perp} = \frac{\partial^2}{\partial x^2} + \frac{\partial^2}{\partial y^2}$.

Because it is assumed that the refractive index varies only in the transverse directions in a single space step, the z -derivatives in (11) commute with the \bar{Z} operator, and the equation is constant coefficient in z . Thus it can be factored into right- and left-going wave operators

$$\left[\frac{d}{dz} + ik_0 n_0 \left(\mathbf{I} + \sqrt{\mathbf{I} + \bar{Z}} \right) \right] \left[\frac{d}{dz} + ik_0 n_0 \left(\mathbf{I} - \sqrt{\mathbf{I} + \bar{Z}} \right) \right] \hat{\mathbf{w}} = 0. \quad (13)$$

Discarding the factor corresponding to the left-going wave in (13), and thus explicitly neglecting backscatter, the pseudo-differential equation form of the propagator results

$$\left[\frac{d}{dz} + ik_0 n_0 \left(\mathbf{I} - \sqrt{\mathbf{I} + \bar{Z}} \right) \right] \hat{\mathbf{w}} = 0, \quad (14)$$

which will be useful to rewrite slightly as

$$\frac{1}{ik_0 n_0} \frac{d}{dz} \hat{\mathbf{w}} + \hat{\mathbf{w}} = \sqrt{\mathbf{I} + \bar{Z}} \hat{\mathbf{w}}. \quad (15)$$

Equation (15) is one form of the propagator, and historically, it appeared first in ocean acoustics [9], though the definition of \bar{Z} is different in that context. Since (14) is constant coefficient in z , it can be formally integrated [10] over a single space step, Δz , to produce a second, exponential operator form of the one-way, one-step, vector propagator

$$\hat{\mathbf{w}}(x, y, z + \Delta z) = e^{iK(-\mathbf{I} + \sqrt{\mathbf{I} + \bar{Z}})} \hat{\mathbf{w}}(x, y, z), \quad (16)$$

where $K = k_0 n_0 \Delta z$ is the non-dimensional space step. This second form of the propagator is explicitly dependent upon K , but this same parameter will appear in any integration scheme developed for the first propagator form in (15).

In this paper we primarily discuss, and implement, the exponential operator form of the propagator. However, there may be some accuracy advantages to be gained using the pseudo-differential propagator, and these are considered in a later section of the paper. In both propagators, variation of the refractive index in the propagation direction is implemented by updating $n(x, y)$ and $\psi(x, y)$ in the \bar{Z} matrix for each new space step. The size of this space step must be at least fine enough to resolve the scale of any inhomogeneities encountered in the z -direction. However it may be finer still, if analysis requires, and an example of such super-resolution is shown in Section 5 of the paper.

Let us establish some notation first, and write (a, b) to denote a rational approximation of numerator degree a and denominator degree b . Our practical computational implementation of the exponential propagator (16) begins with construction of an (N, N) rational approximation in \bar{Z} of the function consisting of the exponential of the square root:

$$\exp\left(iK \sqrt{\mathbf{I} + \bar{Z}}\right) \approx \frac{\sum_{k=0}^N \alpha_{kN} \bar{Z}^k}{\sum_{k=0}^N \beta_{kN} \bar{Z}^k}. \quad (17)$$

We then decompose this rational approximation into partial fractions

$$\frac{\sum_{k=0}^N \alpha_{kN} \bar{Z}^k}{\sum_{k=0}^N \beta_{kN} \bar{Z}^k} = \frac{\alpha_{NN}}{\beta_{NN}} + \sum_{k=1}^N \frac{a_{kN}}{\bar{Z} - b_{kN} \mathbf{I}}. \quad (18)$$

Employing this decomposition, the approximate propagator can be cast in terms of solving multiple linear systems. Defining the N auxiliary variables

$$\overline{\mathbf{W}}_k = e^{-iK} \frac{a_{kN}}{\overline{\mathbf{Z}} - b_{kN}\mathbf{I}} \hat{\mathbf{w}}(x, y, z), \quad (19)$$

we write the approximate propagator as

$$\hat{\mathbf{w}}(x, y, z + \Delta z) \approx e^{-iK} \frac{\alpha_{NN}}{\beta_{NN}} \hat{\mathbf{w}}(x, y, z) + \sum_{k=1}^N \overline{\mathbf{W}}_k. \quad (20)$$

For each k , $\overline{\mathbf{W}}_k$ is found by solving the linear system

$$(\overline{\mathbf{Z}} - b_{kN}\mathbf{I}) \overline{\mathbf{W}}_k = e^{-iK} a_{kN} \hat{\mathbf{w}}(x, y, z). \quad (21)$$

In practice, each of the N versions of (21) is a large, sparse linear system, whose solution is obtained using GMRES.

The accuracy and range of the rational approximation to the exponential operator is clearly an important part of this algorithm's construction. Padé approximants have been the historical choice for this construction, but we adopt a recently introduced interpolation method [31] that gives greater accuracy over a greater range of $\overline{\mathbf{Z}}$. Details are supplied in the next section of the paper.

3 Rational Approximations for Pseudo-differential and Exponential Operator Propagators

An essential stage in implementing both the exponential (16) and pseudo-differential (15) forms of the propagator is generating rational approximations of the factor involving $\sqrt{\mathbf{I} + \overline{\mathbf{Z}}}$, and then decomposing that rational expression into partial fractions. The established procedure [9, 10, 15] for this construction first derives a suitably accurate scalar rational approximation of either $\sqrt{1 + \zeta}$ or $\exp(iK \sqrt{1 + \zeta})$ in the complex ζ plane. Accuracy is particularly required along the real axis, but for waveguide propagation a region above or below the real axis may also be of interest. Following a partial fraction decomposition of this rational approximation, substitution of the $\overline{\mathbf{Z}}$ operator for the surrogate ζ variable produces the desired expression in (18). An appeal to the spectral theory of operators [15] then demonstrates that the accuracy of the spectrum of either $\sqrt{\mathbf{I} + \overline{\mathbf{Z}}}$ or $\exp(iK \sqrt{\mathbf{I} + \overline{\mathbf{Z}}})$ has been equally well preserved by these approximations. This result is possibly more accessible by examining when $\overline{\mathbf{Z}}$ is discretized. For this case the relationship between the individual eigenvalues, $\lambda_i^{\overline{\mathbf{Z}}} \in \text{spec}(\overline{\mathbf{Z}})$, and those of the exponential operator, $\lambda_i^{eH} \in \text{spec}[\exp(iK(-\mathbf{I} + \sqrt{\mathbf{I} + \overline{\mathbf{Z}}}))]$, is given by [18]

$$\lambda_i^{eH} = e^{iK(-1 + \sqrt{1 + \lambda_i^{\overline{\mathbf{Z}}})}. \quad (22)$$

Equation (22) demonstrates that the accuracy of the spectra of the exponential operator is a direct function of the scalar accuracy of the original rational approximation of $\exp(iK \sqrt{1 + \zeta})$.

The range of ζ over which the original rational approximations require accuracy can be estimated by examining the action of the exponential operator propagator upon the family of plane waves admitted by a single component/scalar version of (11) for uniform refractive index fields. In this case $\overline{\mathbf{Z}} = \Delta_{\perp}/k_0^2 n_0^2$, and for an initial condition of the form $w_0(x, y, 0) = \exp(i(k_x x + k_y y))$, the propagator is written

$$w(x, y, \Delta z) = \exp\left(iK \left(-1 + \sqrt{1 - \frac{k_x^2 + k_y^2}{k_0^2 n_0^2}}\right)\right) w_0(x, y, 0) = \exp(ik_z \Delta z) w_0(x, y, 0), \quad (23)$$

where k_z is the z wavenumber calculated from the dispersion relation obtained by substituting a plane wave solution, $w(x, y, z) = \exp(i(k_x x + k_y y + k_z z))$, into the scalar, free space version of (11). The action of \bar{Z} is scalar (and pointwise) for these plane wave initial conditions, and the argument of the exponential in the middle term in (23) is seen to equal the expected $ik_z \Delta z$. Thus, the propagator imposes the pure phase shift experienced by the plane wave propagating over Δz . From this derivation we identify $\Re(\zeta) = -\frac{k_x^2 + k_y^2}{k_0^2 n_0^2}$, where $\Re(\zeta)$ denotes the real part of ζ . Thus $\Re(\zeta) \in [-1, 0]$ for propagating plane waves, and $\Re(\zeta) < -1$ for evanescent plane waves. The remaining terms in \bar{Z} related to the refractive index field can make both positive and negative contributions to the value of ζ within the field. Thus the rational expansion must deliver comparable accuracy for some positive range of $\Re(\zeta)$. As our default, we choose $\Re(\zeta) \in [-4, 2]$ for this overall range, to ensure the rational approximants retain a certain formal accuracy for very wide variations in refractive index, and for waves with wavenumbers of at least $2k_0 n_0$, twice those at the evanescent boundary. This range is double that, $\Re(\zeta) \in [-2, 1]$, previously published [28] in the ocean acoustics literature.

In all previous work we are aware of, Padé expansions of various types were used to initially approximate $\sqrt{1 + \zeta}$ or $\exp(iK \sqrt{1 + \zeta})$. The use of Padé expansions of $\sqrt{1 + \zeta}$ around $\zeta = 0$ was made popular by the description of the analytical form of this expansion's coefficients in [3], and the fact that for $|\zeta| < 1$ some low-order expansions had already appeared in the literature. However, even at that time, there was recognition that both least-squares and interpolation alternatives existed [17] that could offer superior accuracy on the $\Re(\zeta) \in [-1, 0]$ interval that characterizes propagating wave scenarios. The original development of the exponential propagator described here used a Padé approximation shifted to $\zeta = -1$ and then rotated about that point by $\pi/8$ [28]. The shift and rotation caused some accuracy reduction along the $\Re(\zeta)$ axis in $[-1, 0]$, but gained quite reasonable quantitative accuracy in the evanescent region for $\Re(\zeta) < -1$. Here we contrast the accuracy of this older approximant to a new interpolation technique applied to both the exponential and pseudo-differential propagators, and a newly derived Cauchy-integral approximant for the pseudo-differential propagator alone. The new approximants are generally much more accurate than the Padé approximants on the specified accuracy interval $\Re(\zeta) \in [-4, 2]$. In the case of the exponential propagator, the approximation maintains acceptable absolute accuracy, $\mathcal{O}(10^{-8})$, when the Padé approximant has $\mathcal{O}(1)$ errors for multiple-wavelength propagation steps.

3.1 AAA-Lawson interpolation compared to Padé expansion

A new method of rational interpolation in the complex plane was recently introduced in [31], and implemented in the open-source CHEBFUN package [1]. The AAA-Lawson algorithm “first obtains a near-best approximation and a set of support points for a barycentric representation of the rational approximant, then iteratively reweighted least-squares adjustment of the barycentric coefficients is carried out to improve the approximation to minimax”. Customization (shifts, dilations, contractions) of its optimization range for particular applications is easily accomplished using the open-source software. Figure 1 compares the approximation accuracy of partial fraction expansions of a (10, 10) Padé approximant and (25, 25) AAA-Lawson interpolant to $\exp(iK \sqrt{1 + \zeta})$ on $\Re(\zeta) \in [-4, 2]$ when $n_0 = 1.00030$ and $\Delta z = .5\lambda$. The accuracy of the AAA-Lawson partial fraction interpolant is almost uniform across the $\Re(\zeta)$ range, over which the average error is $\sim 2.3 \times 10^{-11}$. The Padé approximant is more accurate around $\zeta = 0$, but is substantially worse everywhere else, and particularly degrades near the branch point of the operator at $\zeta = -1$, which corresponds to the boundary between propagating and evanescent waves. We note that the (10, 10) Padé approximant is at the practical limits of computational accuracy. Higher-order (11, 11) and (12, 12) Padé approximants are no more accurate than that shown, and all order Padé expansions substantially degrade near the branch point. In a serial computational environment it would be justified to argue that the increased accuracy of the AAA-Lawson interpolant has come at the cost of more than doubling the computational effort (i.e., the need to compute 25 subsidiary solutions rather than 10). In a parallel/MPI environment, however, this argument

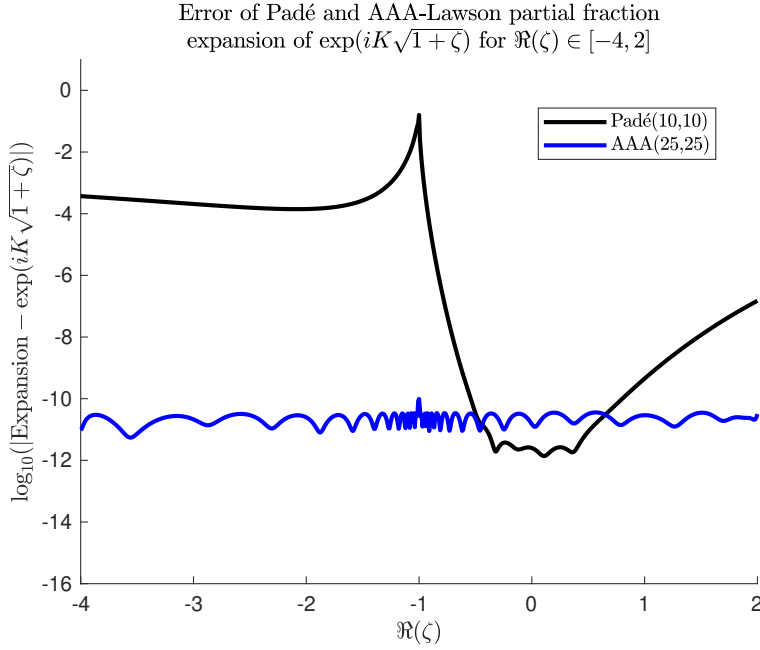


Figure 1: Error of Padé (10,10) and AAA (25,25) partial fraction expansions of $\exp(iK\sqrt{1+\zeta})$, for $\Re(\zeta) \in [-4, 2]$ and $\Delta z = .5\lambda$.

no longer holds, because each term/subsidiary solution will be assigned to its own processor and compute in parallel with all the other terms. In practice there is very little difference in parallel execution time when comparing these two different expansions on the same propagation problems.

The substantial advantage of the AAA-Lawson approximation comes when attempting to approximate the exponential propagation operator for multiple-wavelength propagation steps. Figure 2 compares the approximation accuracy of partial fraction expansions of a (10, 10) Padé and (28, 28) AAA-Lawson approximation of $\exp(iK\sqrt{1+\zeta})$ on $\Re(\zeta) \in [-4, 2]$ when $n_0 = 1.00030$ and $\Delta z = 5\lambda$. Once again, the AAA-Lawson interpolant displays almost uniform accuracy across the range, though errors, which now average $\sim 1.19 \times 10^{-8}$, have increased 3 orders of magnitude compared to the results for the $\Delta z = .5\lambda$ approximation. However, the Padé approximant is an almost complete failure in this case, displaying errors from 5 to 8 orders of magnitude greater than the AAA-Lawson interpolant across the propagating range ($\Re(\zeta) > -1$).

Both Padé and AAA-Lawson approximations are in terms of ζ , but their expansion coefficients are functions of the non-dimensional space step, K , defined after (16). Thus, variations in the value of K due to changes in k_0 , n_0 , or Δz require that new expansion coefficients be generated. For Padé expansion this task was performed by the propagator during its setup phase, using the analytical forms (computer-algebra-generated) of the first 31 Taylor series coefficients of the exponential operator as a function of K . AAA-Lawson interpolants are more robust to these kinds of perturbations, and so a single lookup table may suffice, depending upon the application. Such a lookup table consists of the expansion coefficients for fixed n_0 and varying values of the product $k_0\Delta z$. For EM propagation in air, or the vacuum of space ($n(x, y, z) \in [1.00000, 1.00030]$), a single lookup table using $n_0 = 1.00030$ fills this role.

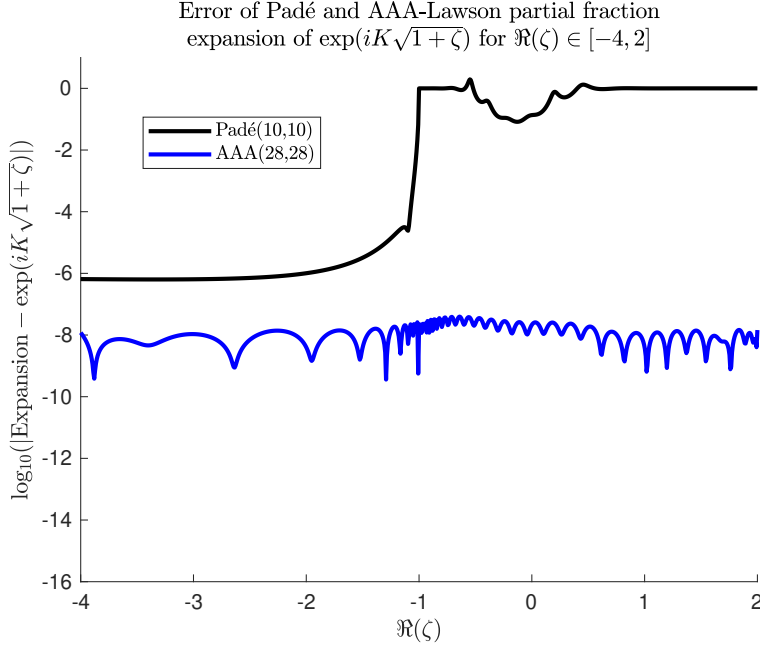


Figure 2: Error of Padé (10,10) and AAA (28,28) partial fraction expansions of $\exp(iK\sqrt{1+\zeta})$, for $\Re(\zeta) \in [-4, 2]$ and $\Delta z = 5\lambda$.

3.2 A Cauchy integral partial fraction approximation

For the pseudo-differential equation form of the propagator (15), we seek a partial fraction approximation of the complex function

$$f(\zeta) = (1 + \zeta)^{1/2}$$

that is valid on the negative real axis and some useful portion of the positive real axis. The branch point $\zeta = -1$ is on the negative real axis, but there is still hope of finding a good approximation away from this branch point. The key step is to transform the branch point at $\zeta = -\infty$ to $w = 1$ via the Möbius transformation

$$w(\zeta) = \frac{\zeta + 1 + i\alpha}{\zeta + 1 - i\alpha} \quad \longleftrightarrow \quad \zeta(w) = -1 + i\alpha \frac{w + 1}{w - 1}. \quad (24)$$

This allows the branch cut in the w plane to be placed on the interval $w \in [-1, 1]$. We then represent the function

$$g(w) = f(\zeta(w)) = \sqrt{\alpha} e^{i\frac{\pi}{4}} (w + 1)^{1/2} (w - 1)^{-1/2}$$

using the Cauchy integral formula

$$g(w) = \frac{1}{2\pi i} \oint_C \frac{g(\xi)}{\xi - w} d\xi, \quad (25)$$

evaluated on a contour that surrounds the new branch cut, and is closed by a circular contour at infinity centered at the origin. A picture of this contour, and the details of the contour integration can be found in Appendix A. The resulting integral representation of $g(w)$ is

$$g(w) = c_\alpha \left(1 - \frac{1}{\pi} \int_{-1}^1 \frac{1}{\eta - w} \sqrt{\frac{1+\eta}{1-\eta}} d\eta \right) \quad c_\alpha = \sqrt{\alpha} e^{i\frac{\pi}{4}}. \quad (26)$$

Noting that the integral has a Jacobi weight function, we approximate it using an N point Gauss-Jacobi quadrature rule,

$$\int_{-1}^1 f(\eta) \sqrt{\frac{1+\eta}{1-\eta}} d\eta \approx \sum_{j=1}^N \omega_j f(\eta_j),$$

where ω_j and η_j are the weights and nodes, respectively, associated with the quadrature rule. For w not on the branch cut, the accuracy/convergence of the Gauss-Jacobi quadrature is $\mathcal{O}(e^{-\rho N})$, where ρ is the sum of major and minor semiaxes of the largest ellipse of analyticity with foci at -1 and 1 . This rate of exponential convergence slows as w approaches the branch cut. For $w = -1$, the singularity is removable and the function is continuous, but with a branch point on the interval; in this case, we expect the convergence to be subexponential with error $\mathcal{O}(N^{-1/2})$.

Inserting the quadrature into the integral expression for g yields

$$g(w) \approx c_\alpha \left(1 - \frac{1}{\pi} \sum_{j=1}^N \frac{\omega_j}{\eta_j - w} \right).$$

Converting from w back to ζ via the Möbius transformation produces

$$\sqrt{1+\zeta} = f(\zeta) \approx c_\alpha \left(1 + \frac{1}{\pi} \sum_{j=1}^N \frac{\omega_j}{1-\eta_j} \frac{1-i\alpha+\zeta}{1+i\alpha\frac{1+\eta_j}{1-\eta_j}+\zeta} \right). \quad (27)$$

We can now use this expression to obtain an approximation for the pseudo-differential equation form of the propagator (15). Let

$$\tilde{\omega}_j = \frac{c_\alpha}{\pi} \frac{\omega_j}{1-\eta_j} \quad \text{and} \quad \sigma_j = \frac{1+\eta_j}{1-\eta_j}.$$

Then the right-hand side of (15) can be expressed as

$$\sqrt{1+\bar{Z}} \hat{w} \approx c_\alpha \hat{w} + \sum_{j=1}^N \tilde{\omega}_j \left((1+i\alpha\sigma_j)\mathbf{I} + \bar{Z} \right)^{-1} \left((1-i\alpha)\mathbf{I} + \bar{Z} \right) \hat{w}. \quad (28)$$

An alternative form is obtained by evaluating the synthetic division of each individual term in the expansion:

$$\sqrt{1+\bar{Z}} \hat{w} \approx \left(c_\alpha + \sum_{j=1}^N \tilde{\omega}_j \right) \hat{w} - \sum_{j=1}^N \frac{i\alpha\tilde{\omega}_j(1+\sigma_j)}{\left((1+i\alpha\sigma_j)\mathbf{I} + \bar{Z} \right)} \hat{w}. \quad (29)$$

The form given by (29) is the closest to that of the partial fraction expansion (18) of the rational approximation of the exponential operator propagator. Using (29) would save a single \bar{Z} multiplication in each auxiliary problem on each propagation step compared to the form in (28).

The accuracy of the expansion in (29) can be seen in Figure 3 confirming the behavior we expect from the analysis above. Here the number of terms is $N = 25$ and the Möbius transformation parameter is set to $\alpha = 1.0$. For comparison we also show the AAA-Lawson expansion of $\sqrt{1+\zeta}$, optimized for the default $\Re(\zeta) \in [-4, 2]$. This expansion has $N = 24$ terms. Except for a narrow band of values around the branch point at $\zeta = -1$, the Cauchy integral expansion is noticeably better than the AAA-Lawson square-root expansion. Note that both these expansions of the pseudo-differential operator are independent of wavelength, refractive index, or propagator space step, in contrast to those for the exponential operator. For fixed N , the width of the low-accuracy band around the branch point can be shrunk substantially by setting $\alpha = 0.1$, but at the cost of reducing the accuracy on either side of the band. To retain the same accuracy

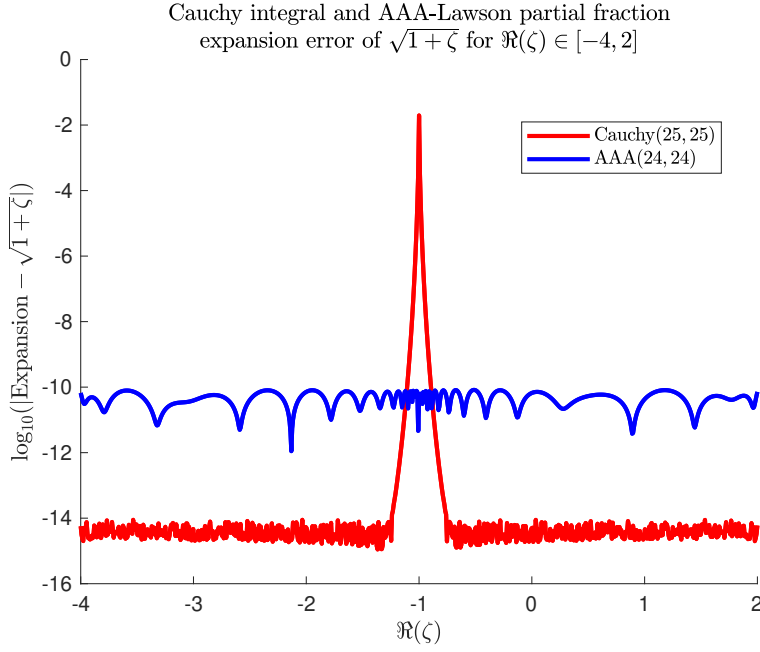


Figure 3: Error of the Cauchy integral(25,25) and AAA-Lawson(24,24) partial fraction expansions of $\sqrt{1+\zeta}$ for $\Re(\zeta) \in [-4, 2]$. $\alpha = 1.0$.

away from the narrowed branch point region, N must be increased to 45. Whether this is a useful trade-off, even in an HPC computing environment, remains to be seen.

As a last step, introduce auxiliary variables \overline{Y}_j and \overline{W}_j to be the solutions of the equations

$$\left((1 + i\alpha\sigma_j)\mathbf{I} + \overline{\mathbf{Z}} \right) \overline{Y}_j = \left((1 - i\alpha)\mathbf{I} + \overline{\mathbf{Z}} \right) \hat{w} \quad (30)$$

$$\left((1 + i\alpha\sigma_j)\mathbf{I} + \overline{\mathbf{Z}} \right) \overline{W}_j = -i\alpha\tilde{\omega}_j(1 + \sigma_j) \hat{w} . \quad (31)$$

Then using (28) and (29), the pseudo-differential equation form of the propagator (15) becomes either

$$\frac{1}{ik_0n_0} \frac{d}{dz} \hat{w} + \hat{w} = c_\alpha \hat{w} + \sum_{j=1}^N \tilde{\omega}_j \overline{Y}_j \quad (32)$$

or

$$\frac{1}{ik_0n_0} \frac{d}{dz} \hat{w} + \hat{w} = \left(c_\alpha + \sum_{j=1}^N \tilde{\omega}_j \right) \hat{w} + \sum_{j=1}^N \overline{W}_j . \quad (33)$$

These can be implemented numerically as alternatives to the approximate propagator (20) coming from the rational approximation of the exponential operator.

4 Numerical Implementation

4.1 Differencing and boundary conditions

Each of the subsidiary variables, \overline{W}_k , in the approximate propagator (20) requires a large sparse linear solve on each propagation step. The coefficient matrices for these solves are composed from a finite difference

representation of the (x, y) derivative terms in the \bar{Z} operator matrix, and updated refractive index fields, if needed. The internal physical domain, gridded $m_{int} \times n_{int}$, is surrounded by Perfectly Matched Layers (PML) of depth m_p and n_p respectively, so that the total computational grid is $(m_{int} + 2m_p - 1) \times (n_{int} + 2n_p - 1) = m \times n$. These wave-damping boundary conditions are applied in the (x, y) directions by modification of the peripheral entries in the second- and first-derivative matrices that apply directly to the transverse electric field components, (w_1, w_2) , across the computational domain. The coefficient matrices involving n^2 and ψ use the same differencing scheme within the physical domain, but their entries are set to zero in the PML layers.

For wave propagation problems on a grid of resolution Δx , the resolving efficiency of a differencing scheme is much more important than its formal order-of-accuracy [24]. Order-of-accuracy describes asymptotic error decrease as $\Delta x \rightarrow 0$; resolving efficiency measures the percentage of available wavenumber bandwidth, $[0, k_{max} = \pi/\Delta x]$, over which a differentiation scheme has no more than a specified relative error with respect to analytical differentiation of a wave. A wave whose derivative is calculated accurately will also have accurate phase and group velocities. The band of dispersive waves correctly propagated on a given grid is the band of waves accurately differentiated on that grid. The differencing schemes for second and first derivatives that our method employs are the fourth-order, explicit, 13-point schemes described in [21] that were originally developed for application to a matrix exponential solver of the paraxial equation. The resolving efficiency of the second derivative matrices at the 99.5% relative accuracy level is 83% of the grid bandwidth, an order of magnitude wider than that attained by standard, 3-point, second-order differencing on the same grid. The PML regions in these differencing matrices use the complex-coordinate transformation paradigm [7, 35, 34, 4, 5]. Further details can be found in [21].

4.2 GMRES iterations and preconditioning

Reference [36] (Section 9.5, page 270) describes the logical structure of a generic, right-conditioned GMRES algorithm, but does not specify the preconditioner, since this choice will be problem dependent. To this algorithm we join a new preconditioner based upon directly solving a free space problem at each GMRES iteration for each \bar{W}_k . For a specified GMRES relative error tolerance no greater than $\tau = 10^{-10}$, the resulting method only requires one iteration for a homogeneous media problem ($\tau < 10^{-13}$), and rarely more than five for inhomogeneous media ($\tau < 10^{-11}$). Its memory usage is minimal, since it does not compute or store any actual matrix decompositions, such as those required by the ILU preconditioning method [36]. In addition, the new GMRES method uses Householder transformations to maintain orthogonalization of the Krylov basis. To the extent that the relative refractive index variation becomes large and continuous within the inhomogeneous propagation domain, more iterations may be required. Numerical results shown later in the paper suggest that iterations begin to increase when there is more than 3% continuous local variation of the underlying refractive index field. Abrupt, isolated changes in the refractive index (e.g. beam transmission through an air-water interface) only locally increase iteration counts. In the next two sections the new preconditioner's physical motivation and actual solution technique are described.

4.2.1 Free space propagation as the preferred preconditioner

There are many approaches to conditioning the iterative solution of a large linear system $Ax = b$. In wave propagation problems it makes sense to search for a preconditioner amongst similar, simpler wave propagation problems that capture the skeleton, or essence, of the more complex propagation scenario under consideration. In the case of both scalar and vector Helmholtz propagation in inhomogeneous media this similar, simpler problem is that of propagation in free space, where the refractive index field is a constant, $n = n_0$. With reference to the structure of the \bar{Z} operator given by (12), the corresponding free space

operator $\bar{\mathbf{Z}}_{fs}$ is

$$\bar{\mathbf{Z}}_{fs} = \frac{1}{k_0^2 n_0^2} \begin{bmatrix} \tilde{\Delta}_\perp & 0 \\ 0 & \Delta_\perp \end{bmatrix} = \begin{bmatrix} \tilde{\Delta}_\perp & 0 \\ 0 & \tilde{\Delta}_\perp \end{bmatrix}, \quad (34)$$

where $\tilde{\Delta}_\perp = (k_0 n_0)^{-2} \Delta_\perp$ is the scaled transverse Laplacian. Note that the free space operator $\bar{\mathbf{Z}}_{fs}$ is characterized solely by the diffraction effects contained in the transverse Laplacian. The heuristic argument is that regardless of the complexity of the three-dimensional refractive index field, the short-range/one-step propagation of the electromagnetic field is characterized, to zeroth order, by how it would propagate through free space. This argument has some similarities to that which underpins the Born approximation, since the now-missing parts of the full $\bar{\mathbf{Z}}$ operator, which depend upon the refractive index variations, are regarded as a perturbation (not necessarily small) on top of the free space propagation. This heuristic motivates the use of $\bar{\mathbf{Z}}_{fs} - b_{kN} \mathbf{I}$ as a preconditioner for the $\bar{\mathbf{Z}} - b_{kN} \mathbf{I}$ coefficient matrices that appear in each of the linear systems (21) for the subsidiary solutions $\overline{\mathbf{W}}_k$.

4.2.2 A Sylvester equation solution of the free space problem

Because the $\bar{\mathbf{Z}}_{fs}$ matrix in (34) is block diagonal in the vector propagation case, the same scalar free space preconditioner will be applied to each electric field component separately during the GMRES iterations for each $\overline{\mathbf{W}}_k$. For component $i = 1, 2$ free space subsidiary fields, $\mathbf{W}_k^{fs}(i)$, on the natural $m \times n$ geometry of the computational field, the general form of these scalar problems is

$$[\tilde{\Delta}_\perp - b_{kN}] \mathbf{W}_k^{fs}(i) = \tilde{\mathbf{D}}_x \mathbf{W}_k^{fs}(i) + \mathbf{W}_k^{fs}(i) \tilde{\mathbf{D}}_y^T - b_{kN} \mathbf{W}_k^{fs}(i) = e^{-iK} a_{kN} \mathbf{w}_i, \quad (35)$$

where $\tilde{\mathbf{D}}_x$ and $\tilde{\mathbf{D}}_y^T$ are the scaled second derivative matrices, including PML boundary conditions, that make up $\tilde{\Delta}_\perp$. Simple matrix algebra then establishes the identity

$$(\tilde{\mathbf{D}}_x - \alpha \mathbf{I}_m) \mathbf{W}_k^{fs}(i) + \mathbf{W}_k^{fs}(i) (\tilde{\mathbf{D}}_y - \beta \mathbf{I}_n)^T = \tilde{\mathbf{D}}_x \mathbf{W}_k^{fs}(i) + \mathbf{W}_k^{fs}(i) \tilde{\mathbf{D}}_y^T - b_{kN} \mathbf{W}_k^{fs}(i) \quad (36)$$

provided $\alpha + \beta = b_{kN}$. The symmetric alternative, $\alpha = \beta = .5b_{kN}$ is chosen here. With this identity, each solution of the component subsidiary field problems in (35) can be obtained from a Sylvester equation

$$(\tilde{\mathbf{D}}_x - .5b_{kN} \mathbf{I}_m) \mathbf{W}_k^{fs}(i) + \mathbf{W}_k^{fs}(i) (\tilde{\mathbf{D}}_y - .5b_{kN} \mathbf{I}_n)^T = e^{-iK} a_{kN} \mathbf{w}_i. \quad (37)$$

These problems can be solved using standard numerical techniques (Bartels & Stewart, Hessenberg-Schur) available in LAPACK, Matlab, Slicot, NAG, etc. The full free space propagator then has the form

$$\mathbf{w}_i(x, y, z + \Delta z) \approx e^{-iK} \frac{\alpha_{NN}}{\beta_{NN}} \mathbf{w}_i(x, y, z) + \sum_{k=1}^N \mathbf{W}_k^{fs}(i). \quad (38)$$

These same preconditioner ideas also apply to solution methods for the subsidiary fields $\overline{\mathbf{Y}}_j$ and $\overline{\mathbf{W}}_j$ that appear in the pseudo-differential forms of the vector propagator shown in (32) and (33).

5 Scalar Computational Results

5.1 The aperture problem and its convergence

A useful theoretical result that tests the functionality of a Helmholtz propagator is the analytical solution of the RS1 integral (3) due to Osterberg and Smith (O&S) [32] describing the transmitted field and intensity on the centerline of a circular aperture illuminated by a normal plane wave. The problem is axisymmetric for

this configuration, and the solution reduces to a single integral over the radial coordinate, $r' = \sqrt{x'^2 + y'^2}$, in the source plane. The centerline intensity has the functional form

$$I(z) = E_0^2 \left[1 + \frac{z^2}{z^2 + a^2} - 2 \frac{z}{\sqrt{z^2 + a^2}} \cos \left(k_0 n_0 [\sqrt{z^2 + a^2} - z] \right) \right], \quad (39)$$

and a corresponding numerical solution of the same integral can be obtained using standard Clenshaw-Curtis (C-C) quadrature [43]. Here E_0 is the incident electric field strength in the aperture, and a is the aperture radius.

In the following we compare the RS1 analytical (O&S) and quadrature (C-C) solutions to the z -axis values of two Helmholtz simulations in which the (x, y) grid resolution either equals, or is less than, a wavelength. In the equals case, the aperture edges are not sharp on the scale of the wavelength, and in the less-than case, they are sharp on the scale of the wavelength. These cases make clear that correct solutions to problems can only occur if all relevant length scales are resolved, and the propagation method is physically correct for those same length scales. Our new propagator naturally satisfies the propagation requirement, in both amplitude and phase, once adequate problem resolution has been specified.

The geometry is a circular aperture of 10λ radius. The physical computational domain is a 60λ square. Propagation extends 120λ in the z direction, and the propagation steps are $\lambda/20$. This super-resolution in the propagation direction is necessary to capture fine details of the diffraction-mediated variation of field and intensity along the axis, despite the refractive index field being constant. The C-C quadratures employ the same number of radial points for computation within the aperture as the Helmholtz propagator uses for finite differencing within the aperture radius, but the former are distributed on a Chebyshev grid, and the latter are uniformly spaced. We expect this to give some accuracy advantage to the C-C quadratures over the propagator results.

Choosing $E_0 = 1$, Figures 4 and 5 display the calculated centerline intensity distributions for the two propagations compared against the analytical solution in (39) and the corresponding C-C quadratures. In Figure 4, the physical transverse grid is 61×61 , so grid resolution is λ and the minimum resolvable scale is 2λ . In wavenumber terms, if $k_0 = 2\pi/\lambda$, the maximum resolved wavenumber when $n = n_0$ is $k_0 n_0/2$. PML layers of 10 grid points complete the computational domain. In Figure 5, the resolution is $\lambda/4$, the minimum resolvable feature size is $\lambda/2$, and the maximum resolved wavenumber is $2k_0 n_0$, well into the evanescent range. The physical grid is now 241×241 , and the PML layers are 40 points wide.

In Figure 4 both the less resolved simulation and the C-C quadrature do a poor job of capturing the analytical behavior at propagation distances less than 20λ . Neither capture the intensity extrema well in this range, but the two methods fail in quite different ways. The Helmholtz propagator gives no extrema at all, while the C-C quadrature calculates two peaks of magnitude greater than 200, well above the plot range. Beyond this initial error zone, the C-C quadrature converges to the analytical solution by 40λ . The propagator solution begins to follow the general trend of the theoretical solution by 40λ , but could not be called converged, given its continuing oscillations about the analytical curve. These variations do decrease with further propagation, but are still visible at twice the distance shown. Note that they are not the result of internal reflections, for quadrupling the depth of the PML layers neither decreases nor eliminates them.

The value and location of the maxima and minima are very sensitive to the complex amplitude of the diffracted waves that reach the centerline. The accuracy of the exponential operator expansions shown in Figures 1 and 2 guarantees that these complex amplitudes are correct for those wavenumbers that are present. The propagator's disagreement with the analytical Rayleigh-Sommerfeld solution is an indication that the ensemble of waves reaching the centerline lack the high wavenumber scales necessary to produce the theoretical interference pattern.

Contrast these results with the more highly resolved, broader wavenumber spectrum, simulation and quadrature in Figure 5. Both propagator and quadrature show excellent agreement with the Rayleigh-Sommerfeld solution from aperture to Fresnel regime, with the quadrature displaying superior accuracy

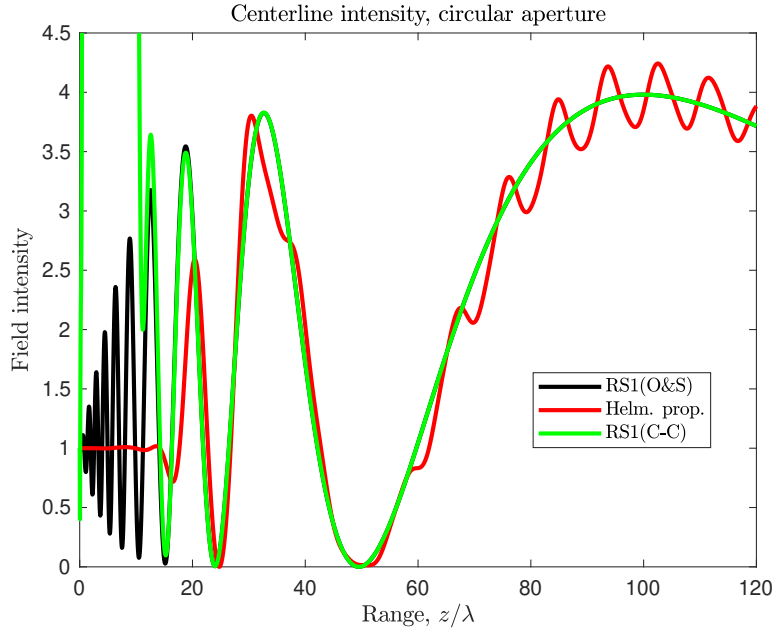


Figure 4: Centerline intensity of a plane wave diffracted by a circular aperture. Comparison of Rayleigh-Sommerfeld theoretical (O&S), (under resolved) Rayleigh-Sommerfeld quadrature (C-C), and new (under resolved) Helmholtz propagator solutions. Transverse grid resolution = λ .

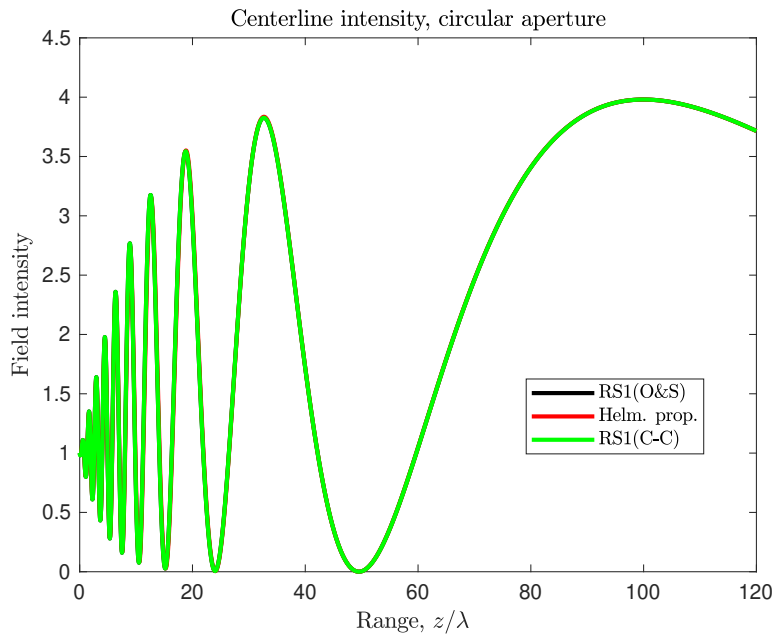


Figure 5: Centerline intensity of a plane wave diffracted by a circular aperture. Comparison of Rayleigh-Sommerfeld theoretical (O&S), Rayleigh-Sommerfeld quadrature (C-C), and new Helmholtz propagator solutions. Transverse grid resolution = $\lambda/4$.

for all but the initial propagation step. The $L2$ norms of the difference between the calculated (propagator, C-C) intensities and the theoretical intensity in (39), normalized by the $L2$ norm of (39), are 6.58×10^{-3} and 6.53×10^{-5} respectively. The band of evanescent wavenumbers in the propagator initial condition cannot contribute to the evolution of the field much beyond a wavelength. However, in the very near field of the aperture, this latter simulation shows that their presence, correctly handled, can make the propagator solution more accurate.

5.2 Convergence of propagator results in transverse planes to quadratures of the Rayleigh-Sommerfeld integral

Analytical, closed-form solutions to the Rayleigh-Sommerfeld integral are rare, and the aperture accuracy results just shown for both propagator simulations and C-C quadratures were only enabled by the existence of the solution in (39). Lacking analytical solutions, additional accuracy and convergence results with respect to other initial conditions can only be obtained by comparison to reference solutions calculated by alternative methods. These may employ denser grids, larger spatial domains, or many more terms, if the reference comes from some sort of expansion or series. Expected greater accuracy is their point, not the computational efficiency of their production. Clenshaw-Curtis quadrature of the RS1 integral showed promise as a source of reference solutions in the last section, and is used here to create transverse reference solutions for Gaussian beams propagated to a single range. An important general advantage of using the RS1 integral to generate reference solutions is that it, and its (non-trigonometric) quadratures, do not suffer from reflection artefacts that result from truncation of an unbounded domain. For the aperture this method displayed higher accuracy than the propagator for essentially the same spatial resolution, and its convergence behavior is quite well characterized as the number of quadrature points increases [43].

The Gaussian beam initial conditions propagated here are created to be narrow enough that their initial spectral content includes wavenumbers in the evanescent range, as the apertured planewave did in the previous section. Such narrow widths also make the beams evolve quickly in space, which decreases the length of propagation required to cause the significant changes in their transverse amplitude needed for useful comparisons at a fixed range. The Fourier-transform pair

$$\frac{1}{2\pi} \int_{-\infty}^{\infty} \int_{-\infty}^{\infty} e^{-(x^2+y^2)/w^2} e^{-i(k_x x + k_y y)} dx dy = \frac{w^2}{2} e^{-(k_x^2 + k_y^2)w^2/4} \quad (40)$$

establishes the usual inverse relation between beam physical and spectral widths. We create two beams, the narrower with a $(1/e)$ spectral width of $k_0 n_0$, and the wider with $(1/e)$ spectral width $.5k_0 n_0$. The corresponding physical widths are $w = \lambda/(\pi n_0)$ and $w = 2\lambda/(\pi n_0)$. Neither beam can have significant energy at wavenumbers beyond $3k_0 n_0$, so they are both gridded at 6-points-per- λ , in line with basic considerations of sampling theory. Both beams were propagated to a distance of $.4\lambda$ using a propagation step of $\lambda/20$. The transverse physical domain of the wider beam was a 20λ square, gridded with 121×121 points, while that of the narrower beam was a 10λ square, gridded with 61×61 points. An additional PML grid of depth 10 surrounded both these physical domains. In the convergence results shown below, the PML depths increased proportional to the grid numbers, so that the physical depth of the PML remained constant.

The Clenshaw-Curtis reference solutions were created using the facilities of the CHEBFUN package [1]. The command `RS1xy = chebfun2(F, [A B C D], 'equi')` creates a two-dimensional Chebyshev interpolant, `RS1xy`, on the $[A, B] \times [C, D]$ domain from the F_{ij} entries of matrix F , with the 'equi' flag signaling that these values are on an equi-spaced grid. Then the command `sum2(RS1xy)` returns the integral of this interpolant on the domain. For an $m_{int} \times n_{int}$ grid of transverse field points (x, y) at propagation distance, $z = z_p$, this two-command sequence was repeated $m_{int} n_{int}$ times to populate the propagated field values at (x, y, z_p) . In each integration, the F_{ij} were values of the RS1 integrand on the source plane grid for a particular value of field point, (x, y, z_p) . Starting with the original propagator grid, the RS1 source grid was successively refined

by factors of 2 until the normalized Frobenius error norm between successive C-C solutions at $z = z_p$ was $O(10^{-14})$. These error norms were based upon differences between complex fields, not their real amplitude or intensity. This is the native output of the RS1 integral, and a multiplication of the propagator envelope solution by $e^{ik_0 n_0 z_p}$ (as in (10)) yields the same quantity. The C-C solution at the last grid refinement was chosen as the reference solution for that particular beam initial condition. The use of powers of 2 for grid refinement meant that propagations on intermediate refined grids could all be checked for convergence to the same reference solution simply by suitable sampling of the reference solution.

A very simplistic comparison between the raw execution times required by the C-C quadratures and the propagator to obtain their beam solutions at $z_p = .4\lambda$ shows that the propagator executes between 15 to 45 times faster than the quadratures, with the speed advantage of the propagator increasing as the grid refinement increased. However, this comparison does not take into account that neither the quadratures nor the propagator were optimized or parallelized. The MATLAB version of the propagator used for these comparisons was serial, used 25 expansion terms (for optimum accuracy), and took 8 steps to get to z_p , while the quadrature calculation did this in one step. A subsequent propagator calculation on the narrow beam showed that its convergence data shown in Figure 7 were barely changed by the use of a single $\Delta z = .4\lambda$ integration step. Thus in a strictly per-step comparison, the propagator would enjoy a further multiplicative speed advantage factor of $200 = 8 \times 25$ over the quadrature when executing in its parallelized version. On the other hand, C-C quadratures are not the only choice for integration of the RS1 integral (e.g. [12, 13, 38, 27, 11]), but there has been no systematic comparison between optimized and parallelized versions of these methods to understand their practical accuracy and computational requirements. Certainly some decrease of execution time should be expected from optimization and parallelization of any RS1 quadrature, but it seems unlikely to be of a magnitude that would bring quadratures to execution-time parity with the propagator. It should also be remembered that RS1 quadratures are only valid for wave propagation in constant refractive index media, not the inhomogeneous media for which the vector propagator has been developed. RS1 quadratures may have advantages for computation of an isolated diffraction field at a single range, but for any application where the development of the intermediate wave field is of interest, they are not competitive with the propagator method in either homogeneous or inhomogeneous media. In addition, the per-step comparison above demonstrates that they are not a useful substitute for our new direct-solve homogeneous media propagator as a preconditioner to GMRES.

For the original source gridding, Figure 6 shows the initial and $z = .4\lambda$ x -axis amplitude profiles of the propagated narrow beam, along with that of its sampled reference solution at the same range. The propagator uses the optimum 25 term expansion of the exponential operator in this solution. To plot resolution, the propagated field and reference solution are indistinguishable. The peak amplitude of the propagated solution is 0.529509, while that of the reference solution is 0.527961. In a similar comparison of the wide beam amplitudes, the propagator and reference solutions are similarly indistinguishable, but the peak amplitudes are now 0.920729 and 0.920087.

Figures 7 and 8 plot the Frobenius difference norm between the Helmholtz propagated beams and their sampled reference solutions, normalized by the Frobenius norm of the sampled reference solution. These relative error norms are shown as a function of both the number of exponential-operator expansion terms and the finite differencing grid employed by the propagator.

Notable for both beams is the insensitivity of the error norms to the number of expansion terms in the propagator once 18 terms are utilized, and this is true regardless of finite differencing resolution. For the same increase in number of expansion terms as shown in the plots, the error norm of the exponential operator expansion for this propagation step decreases by seven orders of magnitude. This suggests that the exponential operator expansion is the most accurate part of the overall numerical method, and that global accuracy is controlled by the finite differencing/discretization error, with possibly some contributions from the PML. The results certainly suggest that fewer than the optimum number of expansion terms could be used in practical computations. This might be advantageous, since fewer processors and less memory would

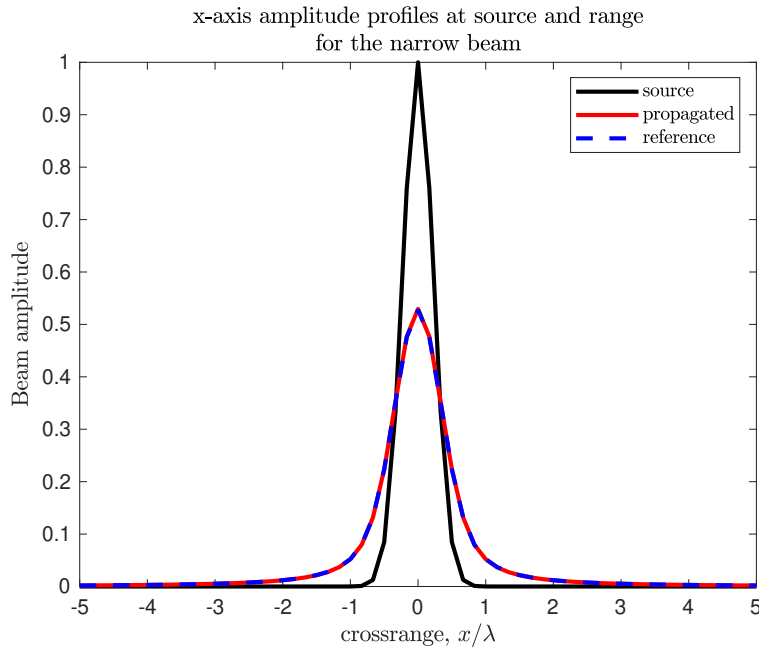


Figure 6: x-axis amplitude profiles of narrow beam at source and $z = .4\lambda$. Comparison of new Helmholtz propagator and Clenshaw-Curtis Rayleigh-Sommerfeld reference solution. Transverse grid 61×61 on $[-5\lambda, 5\lambda]$

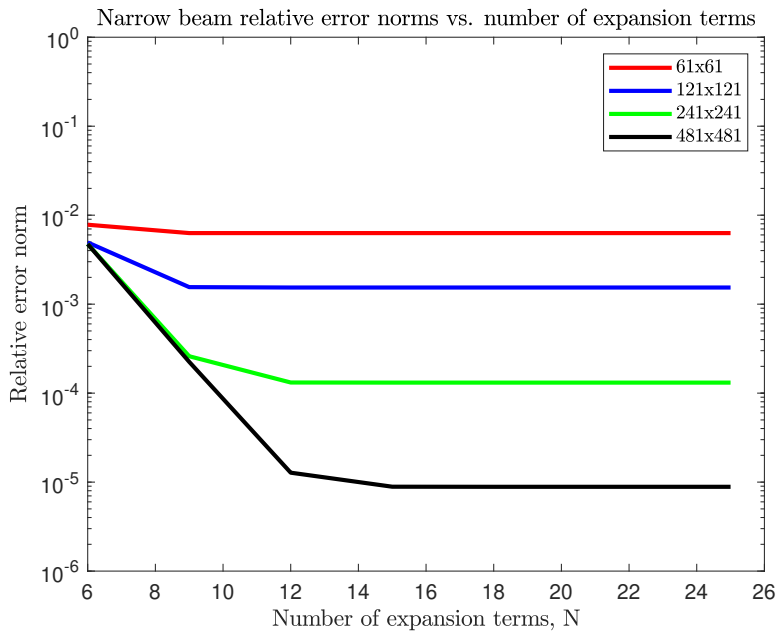


Figure 7: Normalized error norms between the Helmholtz propagated narrow beam and its Clenshaw-Curtis reference solution for variable number of propagator expansion terms and increasingly refined finite difference gridding

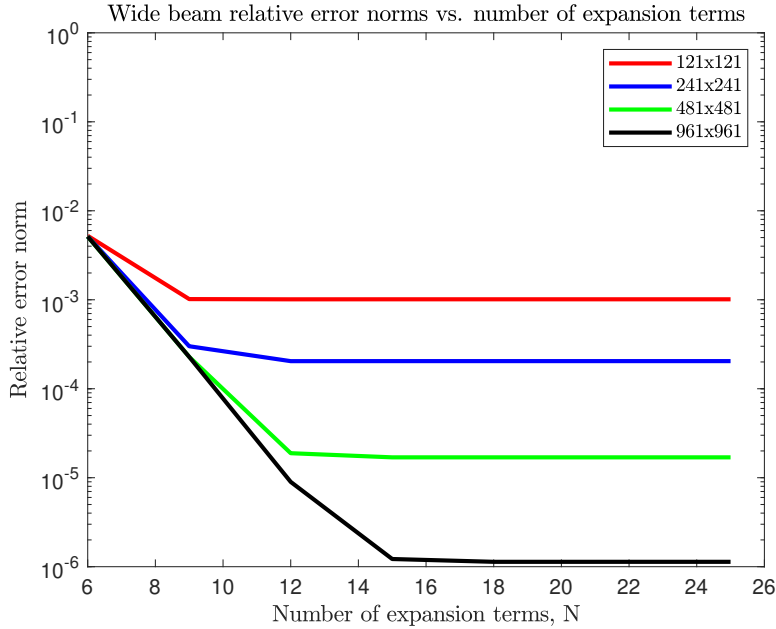


Figure 8: Normalized error norms between the Helmholtz propagated wide beam and its Clenshaw-Curtis reference solution for variable number of propagator expansion terms and increasingly refined finite difference gridding

be required. However, any expectations of a decrease in wall-clock execution time in a parallel computing environment must be tempered by the knowledge that each propagation step cannot occur until the processor(s) calculating the term requiring the most GMRES iterations completes its task. For homogeneous media problems there will be no speed-up, since all terms require a single iteration. For inhomogeneous media propagations, the latter expansion terms typically do require more GMRES iterations per propagation step, but this number must certainly be dependent upon the strength and kind of the inhomogeneities in ways that are difficult to quantify. Maximum GMRES iterations experienced so far are typically 5-8, so it seems unlikely that more than a 20% execution time decrease could be obtained by eliminating calculations of these latter terms in a parallel computing environment.

5.3 Beam propagation through high-wavenumber inhomogeneities

The paraxial equation has been a widely utilized model for EM wave propagation in weakly inhomogeneous media since its introduction in 1946 [25, 26]. Here we contrast beam propagation results from that equation with those from our new Helmholtz propagator in artificially generated refractive index fields. The form of these three-dimensional refractive index fields is that of a rotated sine-product:

$$n(x, y, z) = n_0 + \Delta n \sin(k_s \tilde{x}) \sin(k_s \tilde{y}) \sin(k_s \tilde{z}), \quad (41)$$

where $k_s = k_0 n_0 / (\sqrt{3} q)$, $q \in \{.5, 1, 2\}$, and the rotated tilde system is related to the propagator coordinate system through the axis-angle formulation [33]. In the propagator system the (randomly chosen) rotation axis and angle were, respectively, the unit vector $\hat{u} = (0.258, 0.312, 0.914)$, and the angle 0.128 radians. The selected values of q yield refractive index fields with fundamental wavenumbers of $2k_0 n_0$, $k_0 n_0$, and $.5k_0 n_0$. The reference refractive index value was $n_0 = 1.2$, and the amplitude of the refractive index variations was $\Delta n = 0.025$.

Figures 9, 10, and 12 plot x-axis field amplitude profiles from a collimated Gaussian beam with $(1/e)$ initial width of 25λ , after propagating 240λ through each of the sine-product refractive index fields. These are supplemented by Figures 11 and 13, that show transverse amplitude contours of the two beams after propagation through the two higher wavenumber refractive index fields. The transverse physical domain of these calculations was $120\lambda \times 120\lambda$, with transverse grid sizes of 481×481 for the $.5k_0n_0$ and k_0n_0 refractive index fields and 961×961 for the $2k_0n_0$ refractive index field. PML boundary conditions of 60 or 120 points, respectively, completed the computational domain. Propagation space steps equalled one-quarter of the underlying refractive index field wavelength.

For the same refractive index field the beam amplitude response calculated by the two propagators can be significantly different. The visible effects displayed in these amplitude profiles and contours occur due to at least three related phenomena: differing local response of the beam phase surface to refractive index inhomogeneities; wholesale shifts of the beam centroid away from the (x, y) origin; and non-circular distortion of the beam in planes transverse to the propagation direction.

For the $.5k_0n_0$ refractive index field results shown in Figure 9 there seems little to distinguish the Helmholtz and paraxial beams at this propagation range. However, a calculation of the beam centroids at the end of the propagation shows that the paraxial centroid remains very close to the (x, y) origin at $(-0.00529, 0.00549)\lambda$, while the Helmholtz centroid has shifted to $(0.217, -0.229)\lambda$. Transverse amplitude contour plots reveal no perceptible non-circular distortion, and for that reason we omit them here.

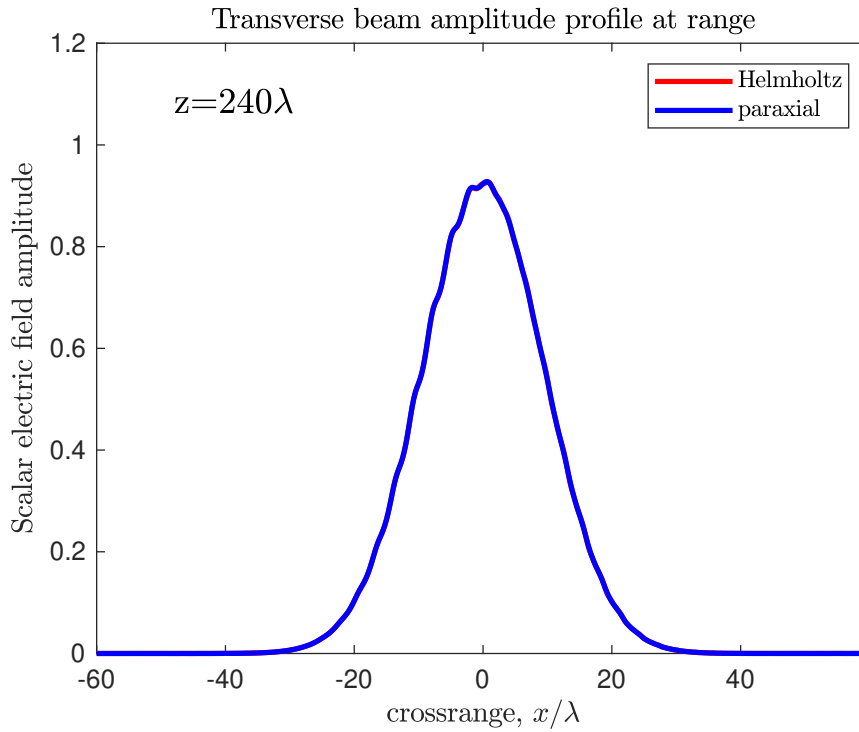


Figure 9: Beam amplitude profiles on the x-axis after 240λ Helmholtz and paraxial propagations through a sine-product refractive index field with a $.5k_0n_0$ fundamental wavenumber

Stronger effects occur for propagations within the k_0n_0 and $2k_0n_0$ refractive index fields. Figure 10 shows the case when the refractive index field length scale equals the fundamental wavelength in the Helmholtz equation. Compared to the paraxial beam, the overall Helmholtz beam amplitude decays more rapidly with propagation distance, and its local fluctuations transverse to the beam are larger. Transverse amplitude

contours are strongly distorted for the Helmholtz beam, but still circular for the paraxial, as can be seen in Figure 11. The Helmholtz beam centroid has shifted to $(9.96, -11.36)\lambda$, while the paraxial centroid remains close to the (x, y) origin at $(0.0113, -0.050)\lambda$.

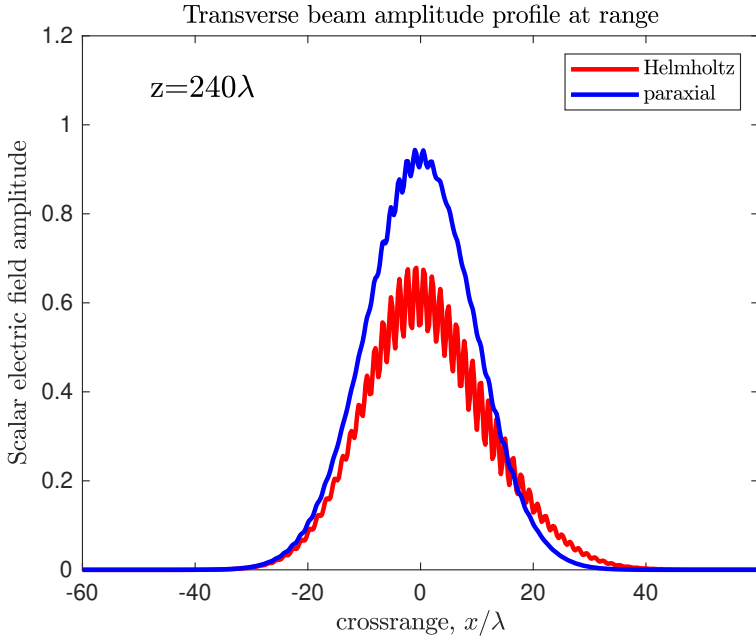


Figure 10: Beam amplitude profiles on the x -axis after 240λ Helmholtz and paraxial propagations through a sine-product refractive index field with a $k_0 n_0$ fundamental wavenumber

The two beams reverse their distortion and shift results for the highest wavenumber refractive index field, shown in Figures 12 and 13. The Helmholtz beam shows only the smallest ripples in amplitude, while the paraxial beam amplitude fluctuates at levels that may exceed those of the Helmholtz beam in the $k_0 n_0$ refractive index field. The Helmholtz beam centroid is very near the (x, y) origin, $(-0.00007, 0.00005)\lambda$, and its amplitude contours are circular. The paraxial beam centroid, on the other hand, has displaced to $(-4.74, -2.93)\lambda$, and its amplitude contours are obviously non-circular, as well as seeming to be distorted in a direction perpendicular to that suffered by the Helmholtz beam within the $k_0 n_0$ refractive index field.

The absence of amplitude fluctuations in the Helmholtz beam within the highest wavenumber refractive index field relates to the evanescent cut-off that occurs in Helmholtz, but not paraxial, propagation. In the $2k_0 n_0$ field the wave-like refractive index perturbations encountered by the Helmholtz beam are at wavenumbers twice those that mark the evanescent boundary of the underlying Helmholtz equation. Thus the electric field phase perturbations they generate are strongly damped in the propagation direction. While continually re-excited as the propagation advances, their effect decays in fractions of a wavelength. The paraxial equation admits no such cut-off, so the refractive index perturbations cause phase perturbations that continue to propagate as undamped waves, interfering with previously excited waves at these frequencies, and contributing to the high level of amplitude fluctuations seen in Figure 12.

6 Discussion

In this paper we have adapted analytical techniques pioneered in the seismology and ocean acoustics communities to the problem of deriving a full vector, one-way wave equation for electromagnetic wave propagation through inhomogeneous refractive index fields. The numerical technology used to implement the

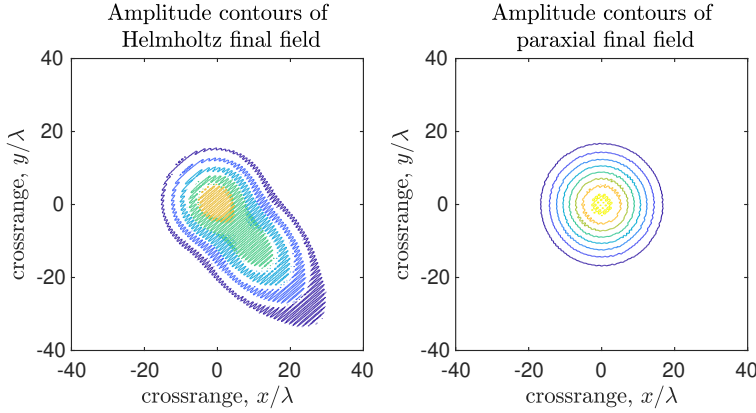


Figure 11: Transverse amplitude contours of Helmholtz and paraxial beams after a $z = 240\lambda$ propagation through a sine-product refractive index field with a $k_0 n_0$ fundamental wavelength

exponential operator form of this vector, one-way Helmholtz equation involves rational approximation, in \bar{Z} , of the exponential operator $\exp(iK \sqrt{1 + \bar{Z}})$, followed by its partial fraction decomposition. This splits the original problem into a moderate number of independent auxiliary problems whose results are summed at each propagation step to advance the electric field in space. The \bar{Z} operator contains all the propagation effects: diffraction, refraction, scattering, and electric field component coupling. Its discretization using high-resolving-efficiency finite differences and PML boundary conditions turns each auxiliary problem into a large, sparse, linear system that is iteratively solved by GMRES and conditioned by the direct solve of a corresponding free space/constant-refractive-index propagation problem that is memory efficient. As an alternative, we have derived the pseudo-differential form of the propagator along with a new Cauchy-integral/partial fraction approximation of the square root operator at its core. In future work we expect to implement this alternative form and test its performance and accuracy against the exponential operator form. This new electromagnetic field propagation method is appropriate for simulating both scalar and vector wave problems involving high-wavenumber refractive index inhomogeneities, or initial conditions with spatial support having wavelength or smaller scales.

Acknowledgements

Approved for public release; distribution is unlimited. Public Affairs release approval # AFRL-2024-4623. This work was supported by AFOSR grant 23RDCOR004. L. Keefe and I. Zilberter acknowledge support from the National Research Council during part of this work. The views expressed are those of the authors and do not necessarily reflect the official policy or position of the Department of the Air Force, the Department of Defense, or the U.S. Government.

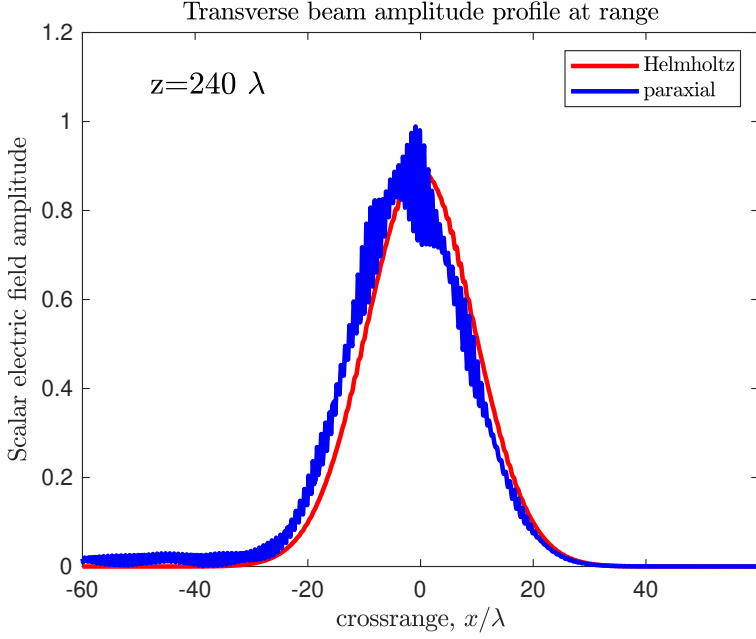


Figure 12: Beam amplitude profiles on the x -axis after 240λ Helmholtz and paraxial propagations through a sine-product refractive index field with a $2k_0n_0$ fundamental wavenumber

A

We complete the Cauchy integral approximation of $f(\zeta) = (1 + \zeta)^{1/2}$ in this section. The Möbius transformation (24) maps the real line into a part of the unit circle. The free parameter $\alpha > 0$ has the effect of moving the point $\zeta = -1 - i\alpha$ to the origin. The origin, in turn, is moved to the point

$$w_\alpha = \frac{1 + i\alpha}{1 - i\alpha}.$$

The segment $(-\infty, -1)$ is moved to the half circle below the real axis and the segment $(-1, 0)$ is moved to the circular arc from -1 to w_α in the upper half plane. This geometry is shown in Fig. 14. As α goes to zero, the point w_α moves closer to 1, enlarging the arc in the upper half plane. Conversely, α going to infinity moves the point w_α closer to -1 , shrinking the arc. It follows that choosing a smaller value of α will improve the approximation near the branch point $\zeta = -1$.

To approximate the function

$$g(w) = f(\zeta(w)) = \sqrt{\alpha} e^{i\frac{\pi}{4}} (w + 1)^{1/2} (w - 1)^{-1/2}.$$

with the Cauchy integral formula (25) we first define a new branch cut on $w \in [-1, 1]$ using the local coordinate parameterization

$$w + 1 = r_1 e^{i\theta_1}, \quad w - 1 = r_2 e^{i\theta_2}, \quad \theta_1, \theta_2 \in (-\pi, \pi), \quad (42)$$

so that $g(w)$ is given by

$$g(w) = c_\alpha \sqrt{\frac{r_1}{r_2}} e^{i\frac{\theta_1 - \theta_2}{2}}, \quad c_\alpha = \sqrt{\alpha} e^{i\frac{\pi}{4}}. \quad (43)$$

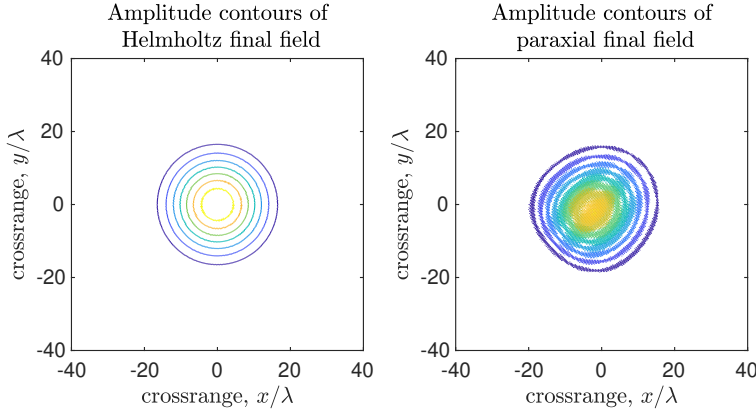


Figure 13: Transverse amplitude contours of Helmholtz and paraxial beams after a $z = 240\lambda$ propagation through a sine-product refractive index field with a $2k_0n_0$ fundamental wavelength

For the Cauchy representation of g to be valid, its integration contour must enclose a region where g is analytic. Take the contour shown in Fig. 15, so that

$$g(w) = \frac{1}{2\pi i} \left(\int_{C_R} + \int_{C_{\varepsilon,1}} + \int_{C_1} + \int_{C_{\varepsilon,2}} + \int_{C_2} \right) \frac{g(\xi)}{\xi - w} d\xi,$$

where C_R is the circle of radius R centered at the origin and $C_{\varepsilon,1}$ and $C_{\varepsilon,2}$ are semicircles around -1 and 1 , respectively, of radius ε . We are interested in the limit as $R \rightarrow \infty$ and $\varepsilon \rightarrow 0$.

On C_R we have $\xi = Re^{i\theta}$, $\theta \in (-\pi, \pi)$. Using the local coordinates defined in (42), we have $\xi + 1 \sim Re^{i\theta}$ and $\xi - 1 \sim Re^{i\theta}$. From (43) the function g on the contour is given by $g(\xi) \sim c_\alpha R^{1/2} e^{i\theta/2} R^{-1/2} e^{-i\theta/2} = c_\alpha$. Therefore,

$$\begin{aligned} \int_{C_R} \frac{g(\xi)}{\xi - w} d\xi &\sim c_\alpha \int_{-\pi}^{\pi} \frac{1}{Re^{i\theta} - w} (iRe^{i\theta} d\theta) \\ &\sim c_\alpha i \int_{-\pi}^{\pi} d\theta \\ &= 2\pi c_\alpha i. \end{aligned}$$

On $C_{\varepsilon,2}$ we have $\xi = 1 + \varepsilon e^{i\theta}$, $\theta \in (\pi/2, -\pi/2)$, so that $\xi + 1 \sim 2$ and $\xi - 1 = \varepsilon e^{i\theta}$, implying $g(\xi) \sim c_\alpha \sqrt{\frac{2}{\varepsilon}} e^{-i\theta/2}$. Therefore,

$$\begin{aligned} \int_{C_{\varepsilon,2}} \frac{g(\xi)}{\xi - w} d\xi &\sim c_\alpha \int_{\pi/2}^{-\pi/2} \frac{\sqrt{\frac{2}{\varepsilon}} e^{-i\theta/2}}{1 + \varepsilon e^{i\theta} - w} (i\varepsilon e^{i\theta} d\theta) \\ &\sim -ic_\alpha \sqrt{2\varepsilon} \int_{-\pi/2}^{\pi/2} \frac{e^{i\theta/2}}{1 + \varepsilon e^{i\theta} - w} d\theta \\ &\rightarrow 0. \end{aligned}$$

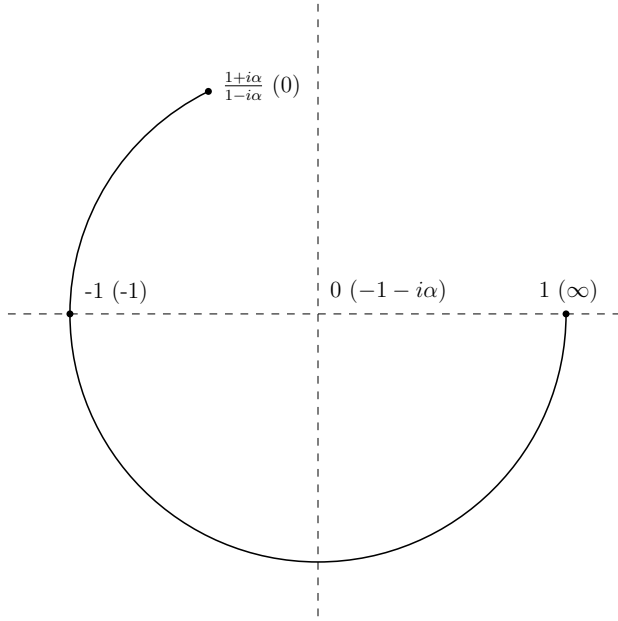


Figure 14: The w -plane corresponding to the Möbius transformation given by equation (24). The bold circular arc is the image of the negative real line. For labeled points, the values in parentheses are the corresponding pre-image points in the ζ -plane.

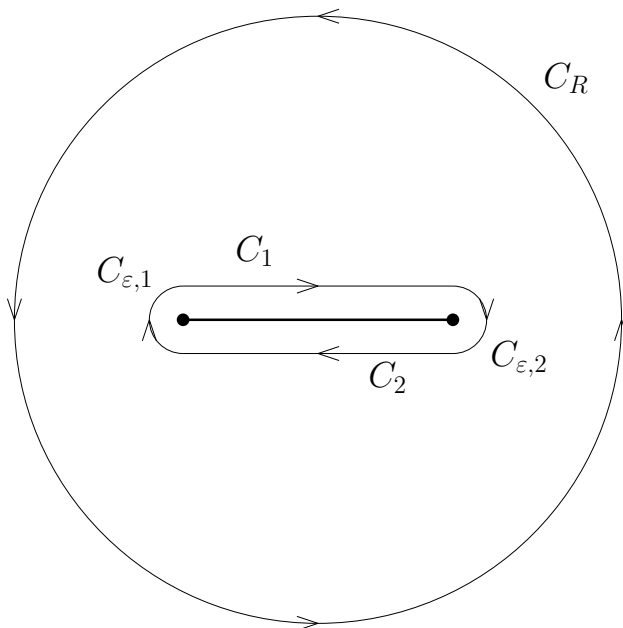


Figure 15: The contour used in the application of Cauchy's integral formula for the function $g(w)$. The bold line segment corresponds to the branch cut, from $[-1, 1]$.

Similarly, $\int_{C_{\varepsilon,1}} \rightarrow 0$.

On C_1 as $\varepsilon \rightarrow 0$ we have $\xi = \eta$ where η goes from -1 to 1, $\theta_1 = 0$, and $\theta_2 = \pi$, implying $g(\xi) = c_\alpha \sqrt{\frac{1+\eta}{1-\eta}} e^{-i\pi/2} = -ic_\alpha \sqrt{\frac{1+\eta}{1-\eta}}$. Therefore,

$$\int_{C_1} \frac{g(\xi)}{\xi - w} d\xi = -ic_\alpha \int_{-1}^1 \frac{1}{\eta - w} \sqrt{\frac{1+\eta}{1-\eta}} d\eta.$$

On C_2 as $\varepsilon \rightarrow 0$ we have $\xi = \eta$ where η goes from 1 down to -1, $\theta_1 = 0$, and $\theta_2 = -\pi$, implying $g(\xi) = c_\alpha \sqrt{\frac{1+\eta}{1-\eta}} e^{i\pi/2} = ic_\alpha \sqrt{\frac{1+\eta}{1-\eta}}$. Therefore,

$$\begin{aligned} \int_{C_2} \frac{g(\xi)}{\xi - w} d\xi &= ic_\alpha \int_1^{-1} \frac{1}{\eta - w} \sqrt{\frac{1+\eta}{1-\eta}} d\eta \\ &= -ic_\alpha \int_{-1}^1 \frac{1}{\eta - w} \sqrt{\frac{1+\eta}{1-\eta}} d\eta. \end{aligned}$$

Combining results, as $R \rightarrow \infty$ and $\varepsilon \rightarrow 0$, we have

$$g(w) = c_\alpha \left(1 - \frac{1}{\pi} \int_{-1}^1 \frac{1}{\eta - w} \sqrt{\frac{1+\eta}{1-\eta}} d\eta \right). \quad (44)$$

References

- [1] Chebfun. <https://www.chebfun.org>, 2022.
- [2] L. C. Andrews and R. L. Phillips. *Laser Beam Propagation Through Random Media*. SPIE, Bellingham, WA, 2005.
- [3] A. Bamberger, B. Engquist, L. Halpern, and P. Joly. Higher order paraxial wave equation approximation in heterogeneous media. *SIAM J. Appl. Math.*, 48:129–154, 1988.
- [4] E. Bécache and P. Joly. On the analysis of Bérenger’s perfectly matched layers for Maxwell’s equations. *ESAIM Math. Model. Numer. Anal.*, 36(1):87–119, 2002.
- [5] E. Bécache, P.G. Petropoulos, and S.D. Gedney. On the long-time behavior of unsplit perfectly matched layers. *IEEE Trans. Antennas Propag.*, 52(5):1335–1342, 2004.
- [6] M. Born and E. Wolf. *Principles of Optics*. Cambridge University Press, Cambridge, 1999.
- [7] W. C. Chew and W. H. Weedon. A 3D perfectly matched medium from modified Maxwell’s equations with stretched coordinates. *Microw. Opt. Technol. Lett.*, 7:599–604, 1994.
- [8] J.F. Claerbout. *Fundamentals of Geophysical Data Processing with Application to Petroleum Prospecting*. McGraw-Hill, New York, 1976.
- [9] M.D. Collins. Application and time-domain solution of higher-order parabolic equations in underwater acoustics. *J. Acoust. Soc. Am.*, 86(3):1097–1102, 1989.
- [10] M.D. Collins. A split-step Padé solution for the parabolic equation method. *J. Acoust. Soc. Am.*, 93:1735–1742, 1993.

- [11] M. Cubillos and E. Jimenez. Diffraction integral computation using sinc approximation. *Appl. Num. Math.*, 178:69–83, 2022.
- [12] A. Dubra and J. Ferrari. Diffracted field by an arbitrary aperture. *Am. J. Phys.*, 67:87–92, 1999.
- [13] G. D. Gillen and S. Guha. Modeling and propagation of near-field diffraction patterns: A more complete approach. *Am. J. Phys.*, 72(9):1195–1201, 2004.
- [14] J.W Goodman. *Introduction to Fourier Optics*. Roberts&Company, Englewood, CO, 3rd edition, 2005.
- [15] R.R. Greene. The rational approximation to the acoustic wave equation with bottom interaction. *J. Acoust. Soc. Am.*, 76:1764–1773, 1988.
- [16] G. R. Hadley. Wide angle beam approximation using Padé approximant operators. *Opt. Lett.*, 17(20):1426–1428, 1992.
- [17] L. Halpern and L.N. Trefethen. Wide-angle one-way wave equations. *J. Acoust. Soc. Am.*, 84:1397–1404, 1988.
- [18] N.J. Higham. *Functions of Matrices*. SIAM, Philadelphia, 2005.
- [19] F.B. Jensen, W.A. Kuperman, M.B. Porter, and H. Schmidt. *Computational Ocean Acoustics*. Springer, New York, 2nd edition, 2011.
- [20] L. R. Keefe, I. Zilberter, and T. Madden. When parabolized propagation fails: A matrix square root propagator for EM waves. *AIAA 2018-3113*, 2018.
- [21] L.R. Keefe. Dispersive waves and PML performance for large-stencil differencing in the parabolic equation. *IEEE Trans. Antennas Propag.*, 60(11):5268–5277, 2012.
- [22] D.L. Knepp. Multiple phase screen calculation of the temporal behavior of stochastic waves. *Proceedings of the IEEE*, 71(6):722–737, 1983.
- [23] M. Koshiha. *Optical Waveguide Analysis*. McGraw-Hill, New York, 1992.
- [24] S.K. Lele. Compact finite difference schemes with spectral-like resolution. *J. Comput. Phys.*, 103:14–42, 1992.
- [25] M.A. Leontovich and V.A. Fock. Solution of propagation of electromagnetic waves along the earth’s surface by the method of parabolic equations. *Soviet Journal of Physics*, 10:13–23, 1946.
- [26] M. Levy. *Parabolic Equation Methods for Electromagnetic Wave Propagation*. Institute of Electrical Engineers, London, 2000.
- [27] R.D. Lewis, G. Beylkin, and L. Monzón. Fast and accurate propagation of coherent light. *Proc. R. Soc. A*, 469(20130323):1195–1201, 2013.
- [28] J. F. Lingeitch and M. D. Collins. Wave propagation in range-dependent poro-acoustic waveguides. *J. Acoust. Soc. Am.*, 104(2):783–792, 1998.
- [29] D. Marcuse. *Light Transmission Optics*. Van Nostrand Reinhold Co., New York, 1972.
- [30] A.S Monin and A.M. Yaglom. *Statistical Fluid Mechanics, Vol. 2*. MIT Press, Cambridge, 1979.

- [31] Y. Nakatsukasa and L. N. Trefethen. An algorithm for real and complex rational minimax approximation. *SIAM J. Sci. Comput.*, 42(5):A3157–A3179, 2020.
- [32] H. Osterberg and L.W. Smith. Closed solutions of Rayleigh’s diffraction integral for axial points. *J. Opt. Soc. Am.*, 51(10):1050–1054, 1961.
- [33] A Palazzolo. Formalism for the matrix of rotations about an arbitrary axis. *Am. J. Phys*, 44(1):63–67, 1976.
- [34] P.G. Petropoulos. Reflectionless sponge layers as absorbing boundary conditions for the numerical solution of Maxwell’s equations in rectangular, cylindrical and spherical coordinates. *SIAM J. Appl. Math.*, 60(3):1037–1058, 2000.
- [35] C. M. Rappaport. Perfectly matched absorbing conditions based on anisotropic lossy mapping of space. *IEEE Microw. Guided Wave Lett.*, 5:90–92, 1995.
- [36] Y. Saad. *Iterative Methods for Sparse Linear Systems*. SIAM, Philadelphia, 2nd edition, 2003.
- [37] D. Schultz, C. Glingener, and E. Voges. Novel generalized finite-difference beam propagation method. *IEEE J. Quant. Electr.*, 30(4):1132–1140, 1994.
- [38] F. Shen and A. Wang. Fast-Fourier-transform based numerical integration method for Rayleigh-Sommerfeld diffraction formula. *Appl. Opt.*, 45(8):1102–1110, 2006.
- [39] J. W. Strohbehn. *Laser Beam Propagation in the Atmosphere*. Springer-Verlag, Berlin, 1978.
- [40] F. Tappert. The parabolic equation method. In J.B. Keller and J.S. Papadakis, editors, *Wave Propagation in Underwater Acoustics*, pages 224–287. Springer-Verlag, New York, 1977.
- [41] V. I. Tatarski. *Wave Propagation in a Turbulent Medium*. McGraw-Hill, New York, 1961.
- [42] V. I. Tatarski, A. Ishimaru, and V. U. Zavorotny. *Wave Propagation in Random Media (Scintillation)*. SPIE-The International Society for Optical Engineering and Institute of Physics Publishing, Bellingham, WA and Bristol, England, 1993.
- [43] L. N. Trefethen. *Approximation Theory and Practice*. SIAM, Philadelphia, extended edition, 2020.
- [44] M.D. White. High-order parabolic beam approximation for aero-optics. *J. Comput. Phys.*, 229:5465–5485, 2010.
- [45] K Yee. Numerical solutions of initial boundary value problems involving maxwell’s equations in isotropic media. *IEEE Trans. Antennas Propag.*, 14(3):302–307, 1966.